

1 ALMA MATER STUDIORUM · UNIVERSITY OF BOLOGNA
2

3

4 School of Science
5 Department of Physics and Astronomy
6 Master Degree in Physics

7

Dataset Generation for the Training of 8 Neural Networks Oriented toward 9 Histological Image Segmentation

10

Supervisor:
Dr. Enrico Giampieri

Co-supervisor:
Dr. Nico Curti

11

Submitted by:
Alessandro d'Agostino

12

Academic Year 2019/2020

¹⁴ **Abstract**

¹⁵ **Abstract.**—The project is inspired by an actual problem of timing and accessibility in
¹⁶ the analysis of histological samples in the health-care system. In this project, I face the
¹⁷ problem of synthetic histological image generation for the purpose of training Neural
¹⁸ Networks for the segmentation of real histological images. The method I propose is
¹⁹ based on the replication of the traditional specimen preparation technique in a virtual
²⁰ environment. The first step is the creation of a 3D virtual model of a region of the
²¹ target human tissue. The model should encapture all the key features of the tissue, and
²² the richer it is the better will be the yielded result. The second step is to perform a
²³ sampling of the model through a virtual sectioning process, which produces a first image
²⁴ of the section, which will act as a segmentation mask. This image is then processed with
²⁵ different tools to achieve a histological-like aspect. The most significant contribution is
²⁶ given by the action of a style transfer neural network that implants the typical visual
²⁷ texture of a histological sample onto the synthetic image. This procedure is presented
²⁸ in detail for two specific models of human tissue: one of pancreatic tissue and one of
²⁹ dermal tissue. The two resulting images compose a pair of images and corresponding
³⁰ ground-truth image, which is perfectly suitable for a supervised learning technique. The
³¹ generation process is completely automatized and does not require the intervention of
³² any human operator, hence it can be used to produce arbitrary large datasets. The
³³ synthetic images are inevitably less complex than the real samples and they offer an
³⁴ easier segmentation task to solve for the NN. However, the synthetic images are very
³⁵ abundant, and the training of a NN can take advantage of this feature, following the
³⁶ so-called curriculum learning strategy.

³⁷ Table of Contents

³⁸	Introduction	6		
³⁹	1 Histological Images Analysis	Theoretical Background	12	
⁴⁰	1.1 Histological Images	12		
⁴¹	1.1.1 Slides Preparation for Optic Microscopic Observation	14		
⁴²	1.2 Introduction to Deep Learning	17		
⁴³	1.2.1 Perceptrons and Multilayer Feedforward Architecture	17		
⁴⁴	1.2.2 Training of a NN - Error Back-Propagation	19		
⁴⁵	1.3 Deep Learning-Based Segmentation Algorithms	25		
⁴⁶	1.3.1 State of the Art on Deep Learning Segmentation	26		
⁴⁷	1.3.2 Image Segmentation Datasets	31		
⁴⁸	2 Technical Tools for Model Development	34		
⁴⁹	2.1 Quaternions	34		
⁵⁰	2.2 Parametric L-Systems	36		
⁵¹	2.3 Voronoi Tassellation	38		
⁵²	2.4 Saltelli Algorithm - Randon Number Generation	40		
⁵³	2.5 Planar Section of a Polyhedron	42		
⁵⁴	2.6 Perlin Noise	44		
⁵⁵	2.7 Style-Transfer Neural Network	45		
⁵⁶	2.8 Working Environment	48		
⁵⁷	3 Tissues Model	Tissue Models	Development	50
⁵⁸	3.1 Pancreatic Tissue Model	50		
⁵⁹	3.1.1 2D Ramification	51		
⁶⁰	3.1.2 Expansion to 3D	52		
⁶¹	3.1.3 Subdivision in Cells	54		

62	3.1.4 Cells Identity Assignment	56
63	3.2 Dermal Tissue Model	57
64	3.3 Synthetic Images Production	61
65	3.3.1 Sectioning Process	61
66	3.3.2 Appearance Makeover	63
67	3.3.3 Alternative Works on Synthetic Histological Images Generation .	68
68	Conclusions	70
69		72
70	Bibliography	73

⁷² Introduction

⁷³ In the last decades, the development of Machine Learning (ML) and Deep Learning (DL)
⁷⁴ techniques has contaminated every aspect of the scientific world, with interesting results
⁷⁵ in many different research fields. The biomedical field is no exception to this and a
⁷⁶ lot of promising applications are taking form, especially as Computer-Aided Detection
⁷⁷ (CAD) systems which are tools for the support of for physicians during the diagnostic
⁷⁸ process. Medical doctors and the healthcare system in general collect a huge amount of
⁷⁹ data from patients during all the treatment, screening, and analysis activities in many
⁸⁰ different shapes, from anographical data to blood analysis to clinical images.

⁸¹ In fact in medicine, the study of images is ubiquitous and countless diagnostic proce-
⁸² dures rely on it, such as X-ray imaging (CAT), nuclear imaging (SPECT, PET), Magnetic
⁸³ resonance, and visual inspection of histological specimens after biopsies. The branch of
⁸⁴ artificial intelligence in the biomedical field that handles image analysis to assist physi-
⁸⁵ cians in their clinical decisions goes under the name of Digital Pathology Image Analysis
⁸⁶ (DPIA). In this thesis work, I want to focus on some of the beneficial aspects intro-
⁸⁷ duced by DPIA in the histological images analysis and some particular issues in the
⁸⁸ development of DL models able to handle this kind of procedure.

⁸⁹ Nowadays the great majority of analysis of histological specimens occurs through
⁹⁰ visual inspection, carried out by highly qualified experts. Some analysis, as cancer
⁹¹ detection, requires the ability to distinguish if a region of tissue is healthy or not with high
⁹² precision in very wide specimens. This kind of procedure is typically very complex and
⁹³ requires prolonged times of analysis besides substantial economic efforts. Furthermore,
⁹⁴ the designated personnel for this type of analysis is often limited, leading to delicate issues
⁹⁵ of priority assignment while scheduling analysis, based on the estimated patient's clinical
⁹⁶ development. Some sort of support to this analysis procedure is therefore necessary.

⁹⁷ The problem of recognizing regions with different features within an image and de-
⁹⁸ tect their borders is known in computer vision as the segmentation task, and it's quite
⁹⁹ widespread with countless different applications, allowing a sort of automatic image in-
¹⁰⁰ terpretation. In ML the segmentation problem is usually faced as a supervised task,
¹⁰¹ hence the algorithm in order to be trained properly requires an appropriate quantity
¹⁰² of pre-labeled images, from which learn the rules through which distinguish different
¹⁰³ regions. This means that the development of segmentation algorithms for a specific ap-

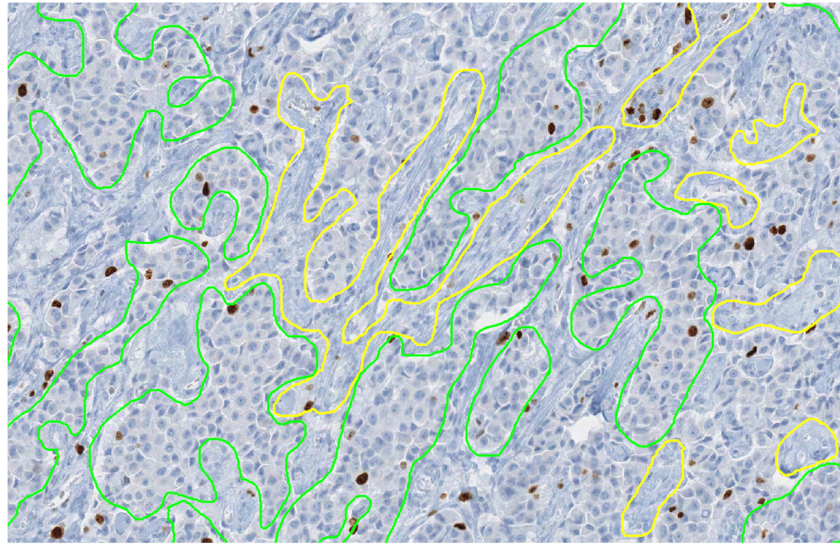


Figure 1: Interleaving of tumor (green annotation) and non-tumor (yellow annotation) regions [28].

104 plication, as would be the one on histological images, would require a lot of starting
105 material, previously analyzed from the same qualified expert encharged of the visual
106 inspection mentioned before. A human operator thus is required to manually track the
107 boundaries, for example, between healthy and tumoral regions within a sample of tissue
108 and to label them with their identity, as in Figure 1. The more the algorithm to train
109 is complex the more starting material is required to adjust the model’s parameters and
110 reach the desired efficacy.

111 The latest developed segmentation algorithms are based on DL techniques, hence
112 based on the implementation of intricated Neural Networks (NN) which process the
113 input images and produce the corresponding segmentation. Those models are typically
114 very complex, with millions of parameters to adjust and tune, therefore they need a
115 huge amount of pre-labeled images to learn their segmentation rules. This need for data
116 is exactly the main focus of my thesis work. The shortage of ground truth images is
117 indeed one of the toughest hurdles to overcome during the development of DL-based
118 algorithms. Another important aspect to bear in mind is the quality of the ground truth
119 material. It’s impossible for humans to label boundaries of different regions with pixel-
120 perfect precision, while for machines the more precise is the input the more effective is
121 the resulting algorithm.

122 Different approaches have already been explored to overcome this problem, and they
123 are mainly based on the generation of synthetic labeled data to use during the training
124 phase. Some techniques achieve data augmentation manipulating already available im-
125 ages and then generating *new* images, but as we will see *later* this approach suffers from

126 different issues. ~~The technique that~~ Here, I want to make an overview of some other
127 interesting works on the generation of synthetic histological images, which have followed
128 completely different paths and strategies from mine.

129 The first work I want to cite is a work from Ben Cheikh *et al.* from 2017 [9]. In
130 this work, they present a methodology for the generation of synthetic images of different
131 types of breast carcinomas. They propose a method completely based on two-dimensional
132 morphology operation, as successive image dilations and erosions. With the modulation
133 of a very restricted number of parameters, regulating the abundance of the objects, their
134 distribution in the image, and their shapes they are able to reconstruct realistic images
135 reflecting different histological situations. In Figure 2 is shown an example of generated
136 material besides a real histological H&E stained sample. Starting from a generated
137 segmentation mask which defines the *tumoral pattern* the production of the synthetic
138 image passes through successive steps, as the generation of characteristic collagen fibers
139 around the structure, the injection of all the immune system cells, and some general final
140 refinements.

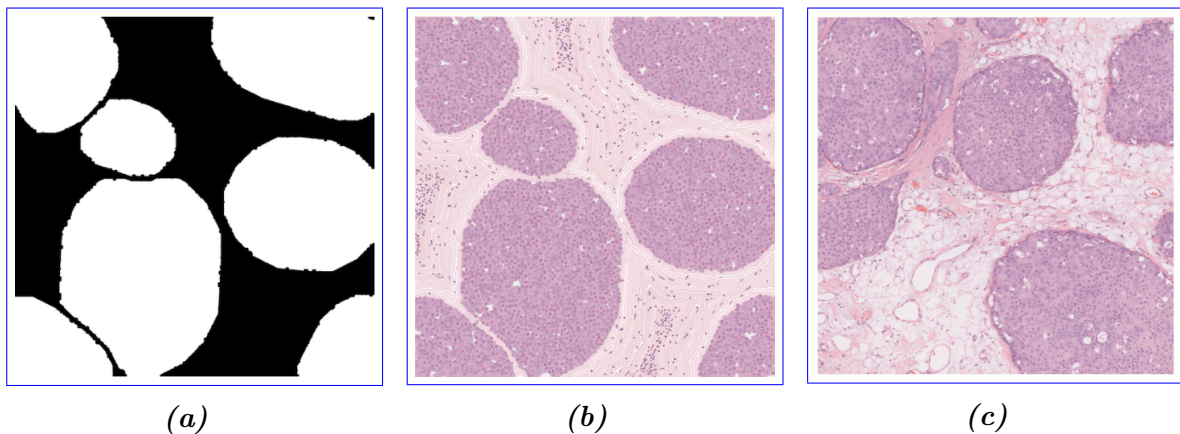


Figure 2: Example of generated tumoral pattern (left), which acts as segmentation mask, of generated image (center) and a real example of the tissue to recreate, from [9].

141 The second work I want to mention is based on a DL-base technique, which approaches
142 synthetic image generation using a specific cGAN architecture inspired to the “U-net”
143 [38] model, as will be described in Figure 1.13 in section 1.3.1. This model works with
144 Ki67 stained samples of breast cancer tissue, and it is able to generate high-fidelity images
145 starting from a given segmentation mask. Those starting segmentation masks tough are
146 obtained through the processing of other real histological samples, via a nuclei-detection
147 algorithm. The differences between real and synthetic samples are imperceptible, and
148 the material generated in this work has effectively fooled experts, who qualified it has
149 indistinguishable from the real one. In Figure 3 an example of a real image, a generated

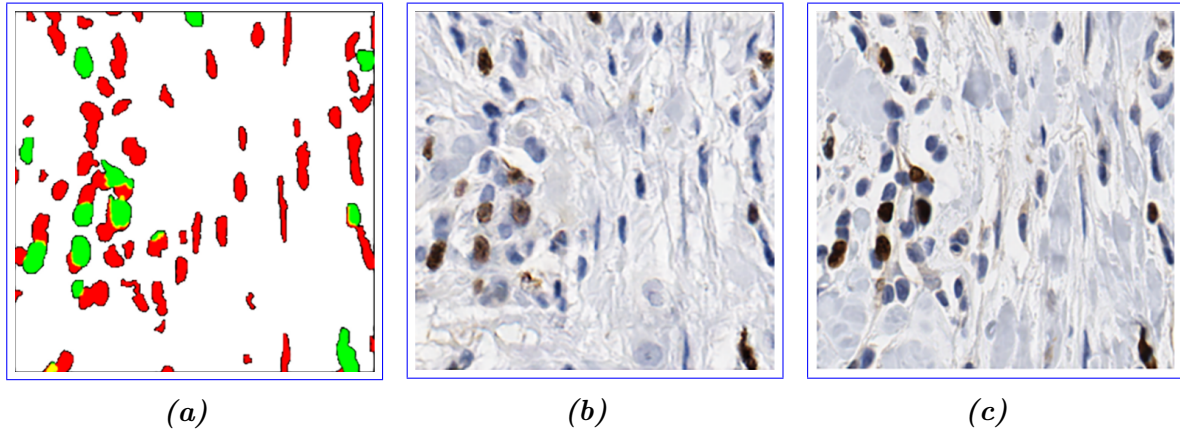


Figure 3: Example of generated tumoral pattern (left), which acts as segmentation mask, of generated image (center) and a real example of the tissue to recreate, from [38].

150 one, and their corresponding segmentation mask.

151 Both of the two before-mentioned strategies produces realistic (or even perfect)
 152 results, but they are based onto considerations and analysis limited only to the aspect
 153 of the images. In the first work, the segmentation mask is produced in an almost
 154 full-random way, while in the second the segmentation mask is extracted starting from
 155 an actual real histological samples. The target of the present work instead lies in between
 156 those two approaches, and wants to produce randomized new images following a plausible
 157 modelization based on physical and histological considerations.

158 The technique I propose in this work follows a generation from scratch of entire
 159 datasets suitable for the training of new algorithms, based on the 3D modelization of a
 160 region of human tissue at the cellular level. The entire traditional sectioning process,
 161 which is made on real histological samples, is recreated virtually on this virtual model.
 162 This yields pairs of synthetic images with their corresponding ground-truth. Using this
 163 technique one would be able to collect sufficient material for the training (the entire phase
 164 or the preliminary part) of a model, overcoming the shortage of hand-labeled data.

165 The 3D modeling of a region of particular human tissue is a very complex task, and it
 166 is almost impossible to capture all the physiological richness of a histological system. The
 167 models I implemented thus are inevitably less sophisticated respect the target biological
 168 structures. I'll show two models: one of pancreatic tissue and another of dermal tissue,
 169 besides all the tools I used and the choices I made during the designing phase.

170 In order to present organically all the steps of my work the thesis is organized in
 171 chapters as follows:

172 **Structure**—[1. Theoretical Background].

173 In this chapter, I will describe how real histological images are obtained and their

174 digitalization process works. Afterward, I will introduce the reader to the Deep
175 Learning framework, explaining the key elements of this discipline and how they
176 work. Finally, I will dedicate a section to the image segmentation problem, and the
177 state of the art of segmentation DL-based algorithms, with particular attention to
178 the applications in the bio-medical field.

179 Of the [2. Technical Tools for Model Development].

180 I will dedicate this chapter to the thorough description of every technical tool I
181 needed during the designing phase of this project. The development has required
182 the harmonization of many different technologies and mathematical tools, some of
183 which not so popular. In this chapter, I will also describe my working environment.

184

185 Thesis-

186 [3. Tissue Models Development].

187 This third chapter is the heart of the project. I will describe in detail all the
188 steps necessary to create the two models, one of pancreatic tissue and the other
189 of dermal tissue, and how I am able to produce the synthetic images. The first
190 section is devoted to the modeling of the histological structures, while the second
191 is entirely dedicated to the sectioning process and the subsequent refinements to
192 the images.

¹⁹⁴ **Chapter 1**

¹⁹⁵ **Histological Images**
¹⁹⁶ **Analysis**Theoretical Background

¹⁹⁷ In this first chapter, I will depict the theoretical context of the work. Section 1.1 will
¹⁹⁸ be dedicated to histological images, and the different techniques used to prepare the
¹⁹⁹ samples to analyze. Histological images recover a fundamental role in medicine and are
²⁰⁰ the pillar of many diagnosis techniques. This discipline borns traditionally from the
²⁰¹ optical inspection of the tissue slides using a microscope, and it is gradually developing
²⁰² and improving with the advent of computers and digital image processing. It is important
²⁰³ tough to understand how the samples are physically prepared, the final target of this
²⁰⁴ work is in fact the virtual reconstruction of this process. In section 1.2 I will introduce
²⁰⁵ the Deep Learning framework and describe how a Neural Network works and actually
²⁰⁶ learns. The most advanced techniques for the automatic image processing implement
²⁰⁷ Deep Learning algorithm, and understanding the general rules behind this discipline is
²⁰⁸ crucial for a good comprehension of this work. In section 1.3 I will discuss in particular
²⁰⁹ the problem of image segmentation and how it is tackled with different Neural Network
²¹⁰ architectures, showing what it is the state of the art of this research field.

²¹¹ **1.1 Histological Images**

²¹² Modern histopathology is essentially based on the careful interpretation of microscopic
²¹³ images, with the intention of correctly diagnose patients and to guide therapeutic de-
²¹⁴ cisions. In the last years, thanks to the quick development of scanning techniques and
²¹⁵ image processing, the discipline of histology have seen radical improvements: the main
²¹⁶ of which undoubtedly is the passage from the microscope's oculars to the computer's
²¹⁷ screen. This digitalization process has brought several advantages, that were previously
²¹⁸ impossible in classical histology, like telepathology and remote assistance in diagnosis
²¹⁹ processes, the integration with other digitalized clinical workflows, and patients' history,

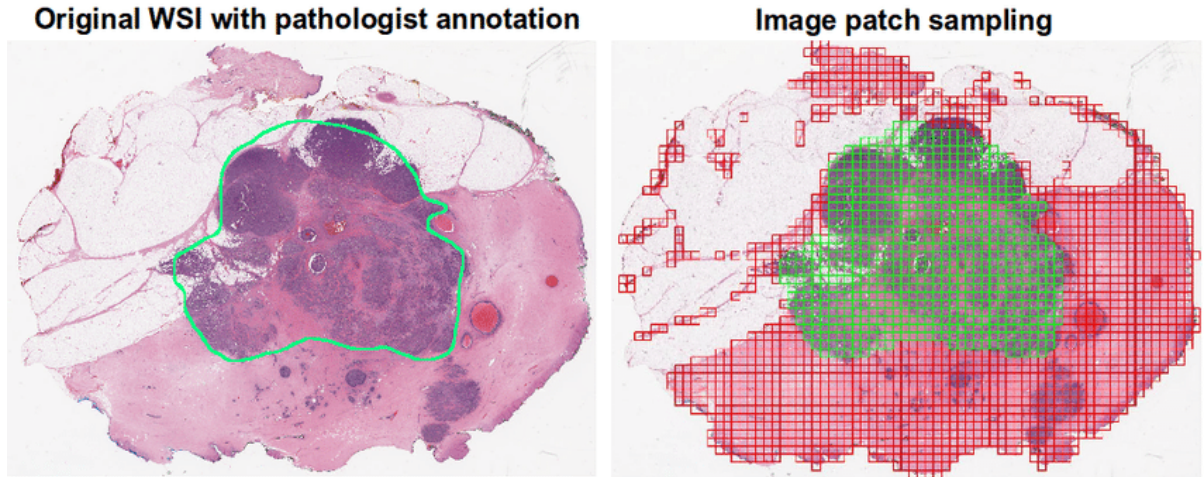


Figure 1.1: An example of whole slide image, with its grid decomposition in patches. It is visible the correspondence between a region of interest manually annotated and the patches that matches that region. From [13]

and most importantly the opening to applications of artificial intelligence. The name Whole Slide Imaging (WSI) refers to the modern virtual microscopy discipline, which consists of scanning a complete microscope slide and creating a single high-resolution digital file. This is commonly achieved by capturing many small high-resolution image tiles or strips and then montaging them to create a full image of a histological section. The four key steps of this process are image acquisition (scansion), editing, and on-screen image visualization.

In the field of Digital Pathology (DP) an essential concept in image understanding is the magnification factor, which indicates the scale of representation of the image and allows dimension referencing. This factor is usually indicated as the magnification power of the microscope's lenses used during the analysis. After the digitalization process, this original magnification factor is prone to change, depending on the resolution of the visualization screen. Therefore, image resolution is measured in μm per pixel, and it is set by the different composition of the acquisition chain, as the optical sensor and the lenses. Histological scanner are usually equipped with $20\times$ or $40\times$ objectives, which correspond to 0.5 and 0.25 mm/pixels resolution values. Lenses with $20\times$ magnification factor are the most suitable for the great majority of histopathological evaluations, and it is the golden standard for scansions, for its good trade-off between image quality and time of acquisition. Scansions with $40\times$ magnification could increase four-fold acquisition and processing time, final file's dimension, and storage cost. A single WSI image, acquired with $20\times$ will occupy more than 600 MB alone.

Despite the WSI is a relatively mature discipline, it still struggles to integrate itself in the standard primitive diagnosis phase in histopathological laboratories. This is primar-

ily due to some disadvantages, like images' resolution, image compression's artifacts, and auto-focusing algorithms, which plays a key role in the specimen interpretation. Furthermore, the scansion of histological samples is an additional step in the analysis which takes time. Despite the technological improvements the average time for the acquisition of a sample is around 5/10 minutes, depending on the number of slices in the slide, for just a single level of magnification. While in traditional histology, the pathologist has access to all the magnification levels at the same time. The real advantage, in fact, is in the long term. Once the images have been acquired they can be archived and consulted remotely almost instantaneously, helping clinical analysis and allowing remote assistance (telemedicine). Furthermore, the images now can be processed by artificial intelligence algorithms, allowing the application of technologies like Deep Learning which could revolutionize the research field, as already has been on many different disciplines in the scientific world.

In order to allow to automatically process, such big images as the ones obtained through WSI, it is necessary to subdivide them in smaller patches. The dimension of which should be big enough to allow interpretation and to preserve a certain degree of representability of the original image. In Figure 1.1 is shown an example of whole slide image, with its grid decomposition in patches. If the patches are too small, it should be over-specified for a particular region of tissue, loosing its general features. This could lead the learning algorithm to misinterpretation. However, this is not an exclusive limit of digital pathology, for a human pathologist would be impossible too to make solid decisions on a too limited sample of tissue. After the subdivision in patches, a typical process for biomedical images is the so-called *data augmentation* of images, that is the process of creating re-newed images from the starting material through simple geometrical transformations, like translation, rotation, reflection, zoom in/out.

The analysis of histological images usually consists in detecting the different components in the samples and to recognise their arrangement as an healthy or pathological pattern. It is necessary to recognize every sign of vitality of the cells, evaluating the state of the nucleus. There are many additional indicators to consider like the presence of inflammatory cells or tumoral cells. Furthermore, samples taken from different parts of the human body present completely different characteristics, and this increase greatly the complexity of the analysis. A reliable examination of a sample thus require a careful inspection made by a highly qualified expert. The automatization of this procedure would be extremely helpful, giving an increadible boost both in timing and in accessibility. However, this is not a simple task and in section 1.3.1 I will show some actual models for biomedical image processing in detail.

1.1.1 Slides Preparation for Optic Microscopic Observation

In modern, as in traditional, histology regardless on the final support of the image the slide has to be physically prepared, starting from the sample of tissue. The sample and

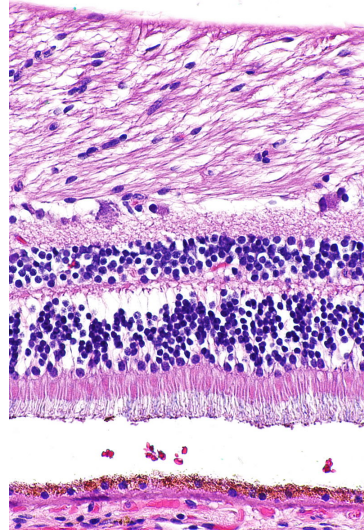


Figure 1.2: A sample of tissue from a retina (a part of the eye) stained with hematoxylin and eosin, cell nuclei stained blue-purple and extracellular material stained pink.

slide preparation is a crucial step for histological or cytological observation. It is essential to highlight what needs to be observed and to *immobilize* the sample at a particular point in time and with characteristics close to those of its living state. There are five key steps for the preparation of samples [4]:

- 282 1) **Fixation** is carried out immediately after the removal of the sample to be observed.
283 It is used to immobilize and preserve the sample permanently in as life-like state
284 as possible. It can be performed immersing the biological material in a formalin
285 solution or by freezing, so immersing the sample in a tissue freezing medium which
is then cooled in liquid nitrogen.
- 291 2) **Embedding** if the sample has been stabilized in a fixative solution, this is the sub-
292 sequent step. It consists in hardening the sample in a paraffin embedding medium,
293 in order to be able to carry out the sectioning. It is necessary to dehydrate the
294 sample beforehand, by replacing the water molecules in the sample with ethanol.
- 295 3) **Sectioning** Sectioning is performed using microtomy or cryotomy. Sectioning is an
296 important step for the preparation of slides as it ensures a proper observation of the
297 sample by microscopy. Paraffin-embedded samples are cut by cross section, using a
298 microtome, into thin slices of $5 \mu m$. Frozen samples are cut using a cryostat. The
299 frozen sections are then placed on a glass slide for storage at $-80^{\circ}C$. The choice of
300 these preparation conditions is crucial in order to minimize the artifacts. Paraffin
301 embedding is favored for preserving tissues; freezing is more suitable for preserving

302 DNA and RNA and for the labeling of water-soluble elements or of those sensitive
303 to the fixation medium.

304 **4) Staining** Staining increases contrasts in order to recognize and differentiate the dif-
305 ferent components of the biological material. The sample is first deparaffinized and
306 rehydrated so that polar dyes can impregnate the tissues. The different dyes can
307 thus interact with the components to be stained according to their affinities. Once
308 staining is completed, the slide is rinsed and dehydrated for the mounting step.

309 Hematoxylin and eosin stain (H&E) is one of the principal tissue stains used in
310 histology [44], and it is the most widely used stain in medical diagnosis and is often
311 the gold standard [35]. H&E is the combination of two histological stains: hematoxylin
312 and eosin. The hematoxylin stains cell nuclei blue, and eosin stains the extracellular
313 matrix and cytoplasm pink, with other structures taking on different shades, hues, and
314 combinations of these colors. An example of H&E stained is shown in Figure 1.2, in
315 which we can see the typical colour palette of an histological specimen.

316 1.2 Introduction to Deep Learning

317 Deep Learning is part of the broader framework of Machine Learning and Artificial
318 Intelligence. Indeed all the problems typically faced using ML can also be addressed
319 with DL techniques, for instance, regression, classification, clustering, and segmentation
320 problems. We can think of DL as a universal methodology for iterative function ap-
321 proximation with a great level of complexity. In the last decades, this technology has
322 seen a frenetic diffusion and an incredible development, thanks to the always increasing
323 available computational power, and it has become a staple tool in all sorts of scientific
324 applications.

325 1.2.1 Perceptrons and Multilayer Feedforward Architecture

326 Like other artificial learning techniques, DL models aim to *learn* a relationship between
327 some sort of input and a specific kind of output. In other words, approximating nu-
328 merically the function that processes the input data and produces the desired response.
329 For example, one could be interested in clustering data in a multidimensional features
330 space, or the detection of objects in a picture, or text manipulation/generation. The
331 function is approximated employing a greatly complex network of simple linear and non-
332 linear mathematical operations arranged in a so-called Neural Network (typically with
333 millions of parameters). The seed idea behind this discipline is to recreate the function-
334 ing of actual neurons in the human brain: their entangled connection system and their
335 “ON/OFF” behavior [41].

336 The fundamental unit of a neural network is called perceptron, and it acts as a digital
337 counterpart of a human neuron. As shown in Figure 1.3 a perceptron collects in input a
338 series on n numerical signals $\vec{x} = 1, x_1, \dots, x_n$ and computes a linear weighted combination
339 with the weights vectors $\vec{w} = w_0, w_1, \dots, w_n$, where w_0 is a bias factor:

$$f(\vec{x}, \vec{w}) = \chi(\vec{x} \cdot \vec{w}). \quad (1.1)$$

340 The results of this linear combination are given as input to a non-linear function $\chi(x)$
341 called the activation function. Typical choices as activation function are any sigmoidal
342 function like $\text{sign}(x)$ and $\tanh(x)$, but in more advanced applications other functions
343 like ReLU [1] are used. The resulting function $f(\vec{x}, \vec{w})$ has then a simple non linear
344 behaviour. It produces a binary output: 1 if the weighted combination is high enough
345 and 0 if it is low enough, with a smooth modulation in-between the two values.

346 The most common architecture for a NN is the so-called *feed-forward* architecture,
347 where many individual perceptrons are arranged in chained layers, which take as input
348 the output of previous layers along with a straight information flux. More complex ar-
349 chitectures could implements also recursive connection, linking a layer to itself, but it
350 should be regarded as sophistication to the standard case. There are endless possibilities

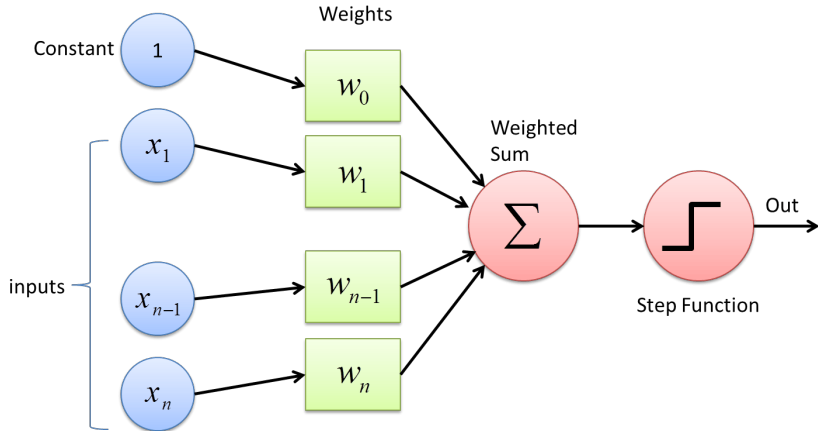


Figure 1.3: Schematic picture of a single layer perceptron. The input vector is linearly combined with the bias factor and sent to an activation function to produce the numerical "binary" output.

of combination and arrangement of neurons inside a NN's layer, but the most simple ones are known as *fully-connected* layers, where every neuron is linked with each other neuron of the following layer, as shown in Figure 1.4. Each connection has its weight, which contributes to modulate the overall combination of signals. The training of a NN consists then in the adjustment and fine-tuning of all the network's weights and parameters through iterative techniques until the desired precision in the output generation is reached.

Although a fully connected network represents the simplest linking choice, the insertion of each weight increases the number of overall parameters, and so the complexity of the model. Thus we want to create links between neurons smartly, rejecting the less useful ones. Depending on the type of data under analysis there are many different established typologies of layers. For example, in the image processing field, the most common choice is the convolutional layer, which implements a sort of discrete convolution on the input data, as shown in Figure 1.5. While processing images, the convolution operation confers to the perception of correlation between adjacent pixels of an image and their color channels, allowing a sort of spatial awareness. Furthermore, the majority of traditional computer vision techniques are based on the discrete convolution of images, and on the features extracted from them.

As a matter of principle a NN with just two successive layers, which is called a *shallow* network, and with an arbitrary number of neurons per layer, can approximate arbitrary well any kind of smooth enough function [32]. However, direct experience suggests that networks with multiple layers, called *deep* networks, can reach equivalent results exploiting a lower number of parameters overall. This is the reason why this discipline goes under the name of *deep* learning: it focuses on deep networks with up

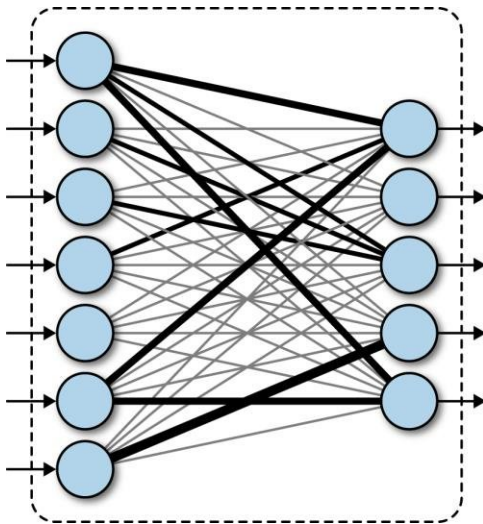


Figure 1.4: Schematic representation of a fully connected (or dense) layer. Every neuron from the first layer is connected with every output neuron. The link thickness represent the absolute value of the combination weight for that particular value.

375 to tens of hidden layers. Such deep structures allow the computation of what is called
 376 deep features, so features of the features of the input data, that allows the network to
 377 easily manage concepts that would be barely understandable for humans.

378 1.2.2 Training of a NN - Error Back-Propagation

379 Depending on the task the NN is designed for, it will have a different architecture and
 380 number of parameters. Those parameters are initialized to completely random values,
 381 tough. The training process is exactly the process of seeking iteratively the right values
 382 to assign to each parameter in the network in order to accomplish the task. The best
 383 start to understanding the training procedure is to look at how a supervised problem is
 384 solved. In supervised problems, we start with a series of examples of true connections
 385 between inputs and correspondent outputs and we try to generalize the rule behind those
 386 examples. After the rule has been picked up the final aim is to exploit it and to apply
 387 it to unknown data, so the new problem could be solved. In opposition to the concept
 388 of supervised problems, there are the *unsupervised* problems, where the algorithm does
 389 not try to learn a rule from a practical example but try to devise it from scratch. A task
 390 typically posed as unsupervised is clustering, when different data are separated in groups
 391 based on the values of their features in the feature space. Usually, only the number of
 392 groups is taken in input from the algorithm, and the subdivision is completely performed
 393 by the machine. In the real world, by the way, there are many different and creative

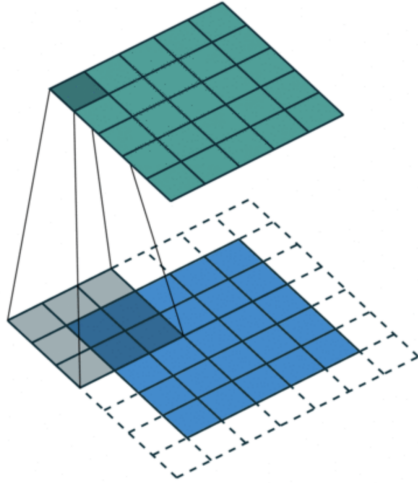


Figure 1.5: Schematic representation of a convolutional layer. The input data are processed by a window kernel that slides all over the image. This operation can recreate almost all the traditional computer vision techniques, and can overcome them, creating new operations, which would be unthinkable to hand-engineered.

394 shapes between pure supervised and pure unsupervised learning, based on the actual
 395 availability of data and specific limitations to the individual task.

396 An interesting mention in this regards should be made about *semi-supervised* learn-
 397 ing, which is typically used in bio-medical applications. This learning technique combines
 398 a large quantity of unlabeled data during training with a limited number of pre-labeled
 399 example. The blend between data can produce considerable improvement in learning
 400 accuracy, and leading to better results respect to pure unsupervised techniques. The
 401 typical situation of usage of this technique is when the acquisition of labeled data re-
 402 quires a highly trained human agent (as an anatomo-pathologist) or a complex physical
 403 experiment. The actual cost of building entire and suitable fully labeled training sets
 404 in these situations would be unbearable, and semi-supervised learnign comes in great
 405 practical help.

406 Another important training technique which worth mentioning is the so-called *curriculum*
 407 *learning* [5]. This is a learning technique inspired by the typical learning curve human
 408 being and animal, that are used to face problems of always increasing difficulty while
 409 learning something new or a new skill. The example presented to the Neural Network are
 410 not randomly presented but organized in a meaningful order which illustrates gradually
 411 more concepts, and gradually more complex ones. The experiments show that through
 412 curriculum learning significant improvements in generalization can be achieved. This
 413 approach has both an effect on the speed of convergence of the training process to a

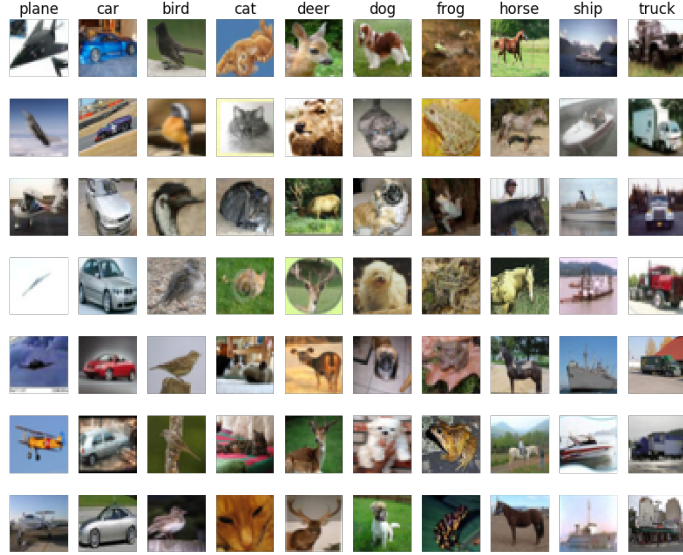


Figure 1.6: Sample grid of images from the CIFAR10 dataset. Each one of the 32×32 image is labeled with one of the ten classes of objects: plane, car, bird, cat, deer, dog, frog, horse, ship, truck.

414 minimum and, in the case of non-convex criteria, on the quality of the local minima
 415 obtained. This technique is of particular interest for this work: the generated images,
 416 which will be shown in section 3.3, will offer a segmentation task much less complex
 417 respect to the analysis of real histological tissue. In the optical of training a DL-based
 418 model the abundantly produced images can be used for the preliminary phase of training,
 419 setting aside the more complex and more valuable hand-labeled images for the finalization
 420 of the training process.

421 A good example of supervised problems tough is the classification of images. Let's
 422 assume we have a whole dataset of pictures of different objects (as cats, dogs, cars, etc.)
 423 like the CIFAR10 [22] dataset. This famous dataset is made of over $60K$ labeled colored
 424 images 32×32 divided into 10 categories of objects as shown in Figure 1.6. We could be
 425 interested in the creation of a NN able to assign at every image its belonging class. This
 426 NN could be arbitrarily complex but it certainly will take as input a $32 \times 32 \times 3$ RGB
 427 image and the output will be the predicted class. A typical output for this problem
 428 would be a probability distribution over all the 10 classes like:

$$\vec{p} = (p_1, p_2, \dots, p_{10}), \quad (1.2)$$

$$\sum_{i=1}^{10} p_i = 1, \quad (1.3)$$

429 and it should be compared with the true label, that is represented just as a binary
 430 sequence \vec{t} with the bit correspondent to the belonging class set as 1, and all the others
 431 value set to 0:

$$\vec{t} = (0, 0, \dots, 1, \dots, 0, 0). \quad (1.4)$$

432 Every time an image is given to the model an estimate of the output is produced.
 433 Thus, we need to measure the *distance* between that prediction and the true value, to
 434 quantify the error made by the algorithm and try to improve the model's predictive
 435 power. The functions used for this purpose are called loss functions. The most common
 436 choice is the Mean Squared Error (MSE) function that is simply the averaged L^2 norm
 437 of the difference vector between \vec{p} and \vec{t} :

$$MSE = \frac{1}{n} \sum_{i=0}^n (t_i - p_i)^2. \quad (1.5)$$

438 Let's say the NN under training has L consecutive layers, each one with its activation
 439 function f^k and its weights vector \vec{w}^k , hence the prediction vector \vec{p} could be seen as the
 440 result of the consecutive, nested, application through all the layers:

$$\vec{p} = f^L(\vec{w}^L \cdot (f^{L-1}(\vec{w}^{L-1} \cdot \dots \cdot f^1(\vec{w}^1 \cdot \vec{x}))). \quad (1.6)$$

441 From both equations 1.5 and 1.6 it is clear that the loss function could be seen as
 442 a function of all the weights vectors of every layer of the network. So if we want to
 443 reduce the distance between the NN prediction and the true value we need to modify
 444 those weights to minimize the loss function. The most established algorithm to do so for
 445 a supervised task in a feed-forward network is the so-called *error back-propagation*.

446 The back-propagation method is an iterative technique that works essentially com-
 447 puting the gradient of the loss function with respect to the weights using the derivative
 448 chain rule and updating by a small amount the value of each parameter to lower the
 449 overall loss function at each step. Each weight is *moved* counter-gradient, and summing
 450 all the contribution to every parameter the loss function approaches its minimum. In
 451 equation 1.7 is represented the variation applied to the j^{th} weight in the i^{th} layer in a
 452 single step of the method:

$$\Delta w_{ij} = -\eta \frac{\partial E}{\partial w_{ij}}, \quad (1.7)$$

453 where E is the error function, and η is the *learning coefficient*, that modulate the effect of
 454 learning through all the training process. This iterative procedure is applied completely
 455 to each image in the training set several times, each time the whole dataset is reprocessed
 456 is called an *epoch*. The great majority of the dataset is exploited in the training phase

457 to keep running this trial and error process and just a small portion is left out (typically
458 10% of the data) for a final performance test.

459 The loss function shall inevitably be differentiable, and its behavior heavily influences
460 the success of the training. If the loss function presents a gradient landscape rich of
461 local minima the gradient descent process would probably get stuck in one of them.
462 More sophisticated algorithms capable of avoiding this issue have been devised, with
463 the insertion of some degree of randomness in them, as the Stochastic Gradient Descent
464 algorithm, or the wide used *Adam* optimizer [21].

465 While Error-Back Propagation is the most established standard in DL applications, it
466 suffers from some problems. The most common one is the so-called vanishing or explod-
467 ing gradient issue, which is due to the iterative chain derivation through all the nested
468 level of composition of the function. Without a careful choice of the right activation
469 function and the tuning of the learning hyper-parameters it is very easy to bump into
470 this pitfall. Furthermore the heavy use of derivation rises the inability to handle non-
471 differentiable components and hinders the possibility of parallel computation. However,
472 there are many alternative approaches to network learning beside EBP. The Minimiza-
473 tion with Auxiliary Variables (MAV) method builds upon previously proposed methods
474 that break the nested objective into easier-to-solve local subproblems via inserting aux-
475 illiary variables corresponding to activations in each layer. Such method avoids gradient
476 chain computation and the potential issues associated with it [10]. A further alterna-
477 tive approach to train the network is the Local Error Signals (LES), which is based on
478 layer-wise loss functions. In [29], is shown that layer-wise training can approach the
479 state-of-the-art on a variety of image datasets. It is used a single-layer sub-networks
480 and two different supervised loss functions to generate local error signals for the hidden
481 layers, and it is shown that the combination of these losses helps with optimization in
482 the context of local learning.

483 The training phase is the pulsing heart of a DL model development and it could
484 take even weeks on top-level computers for the most complicated networks. In fact,
485 one of the great limits to the complexity of a network during the designing phase is
486 exactly the available computational power. There are many more further technical details
487 necessary for proper training, the adjustment of which can heavily impact the quality of
488 the algorithm. However, after the training phase, we need to test the performance of the
489 NN. This is usually done running the trained algorithm on never seen before inputs (the
490 test dataset) and comparing the prediction with the ground-truth value. A good way to
491 evaluate the quality of the results is to use the same function used as the loss function
492 during the training, but there is no technical restriction to the choice of this quality
493 metric. The average score on the whole test set is then used as a numerical score for
494 the network, and it allows straightforward comparison with other models' performances,
495 trained for the same task. All this training procedure is coherently customized to every
496 different application, depending on which the problem is posed as supervised or not and
497 depending on the more or less complex network's architecture. The leitmotif is always

⁴⁹⁸ finding a suitable loss function that quantifies how well the network does what it has
⁴⁹⁹ been designed to do and trying to minimize it, operating on the parameters that define
⁵⁰⁰ the network structure.



Figure 1.7: Example of the resulting segmentation mask of an image of an urban landscape. Every interesting object of the image is detected and a solid color region replaces it in the segmentation mask. Every color corresponds to a different class of objects, for example, persons are highlighted in magenta and scooters in blue. The shape and the boundaries of every region should match as precisely as possible the edges of the objects.

501 1.3 Deep Learning-Based Segmentation Algorithms

502 In digital image processing, image segmentation is the process of recognizing and sub-
 503 dividing an image into different regions of pixels that show similar features, like color,
 504 texture, or intensity. Typically, the task of segmentation is to recognize the edges and
 505 boundaries of the different objects in the image and assigning a different label to every
 506 detected region. The result of the segmentation process is an image with the same dimen-
 507 sions of the starting one made of solid color regions, representing the detected objects.
 508 This image is called *segmentation mask*. In Figure 1.7 is shown an example of segmenta-
 509 tion of a picture of an urban landscape: different colors are linked to different classes of
 510 objects like persons in magenta and scooters in blue. This technology has a significant
 511 role in a wide variety of application fields such as scene understanding, medical image
 512 analysis, augmented reality, etc.

513 A relatively easy segmentation problem, and one of the first to be tackled, could
 514 be distinguishing an object from the background in a grey-scale image, [like in Figure](#)
 515 [1.8](#). The easiest technique to perform segmentation in this kind of problem is based on
 516 thresholding. Thresholding is a binarization technique based on the image's grey-level
 517 histogram: to every pixel with luminosity above that threshold is assigned the color
 518 *white*, and vice versa the color *black*. However, this is a very primitive and fallacious, yet
 519 very fast method, and it manages poorly complex images or images with un-uniformity
 520 in the background.

521 A lot of other traditional techniques improve this first segmentation method [11].
 522 Some are based on the object's edges recognition, exploiting the sharp change in lumi-
 523 nosity typically in correspondence of the boundary of a shape. Other techniques exploit
 524 instead a region-growing technology, according to which some *seed* region markers are



Figure 1.8: Example of the resulting segmentation mask of an image of a fingerprint obtained through a thresholding algorithm. The result is not extremely good, but this technique is very easy to implement and runs very quickly.

scattered on the image, and the regions corresponding to the objects in the image are grown to incorporate adjacent pixels with similar properties.

Every development of traditional computer vision or of Machine Learning-based segmentation algorithm suffers from the same, inevitable limitation. For every one of those techniques is the designing phase in which the operator should decide precisely which features to extract from the image, like different directional derivatives in the image plane or image entropy, and how to process them for the rest of the analysis. There is thus an intrinsic limitation in the human comprehension of those quantities and in the possible way to combine them. The choice is made on the previous experimental results in other image processing works, and on their theoretical interpretation. Neural Networks instead are relieved from this limitation, allowing themselves to learn which features are best suited for the task and how they should be processed during the training phase. The complexity is then moved on to the design of the DL model and on its learning phase rather than on the hand-engineering design of the features to extract. In Figure 1.9 an example high-level feature extracted from a DL model trained for the segmentation of nuclei in a histological sample. The model learns the typical pattern of arrangement of nuclei, which would have been impossible to describe equally in advance.

1.3.1 State of the Art on Deep Learning Segmentation

Similarly to many other traditional tasks, also for segmentation, there has been a thriving development lead by the diffusion of deep learning, that boosted the performances resulting in what many regards as a paradigm shift in the field [27].

In further detail, image segmentation can be formulated as a classification problem of pixels with semantic labels (semantic segmentation) or partitioning of individual objects (instance segmentation). Semantic segmentation performs pixel-level labeling with a set of object categories (e.g. boat, car, person, tree) for all the pixels in the image, hence it is typically a harder task than image classification, which requires just a single label for

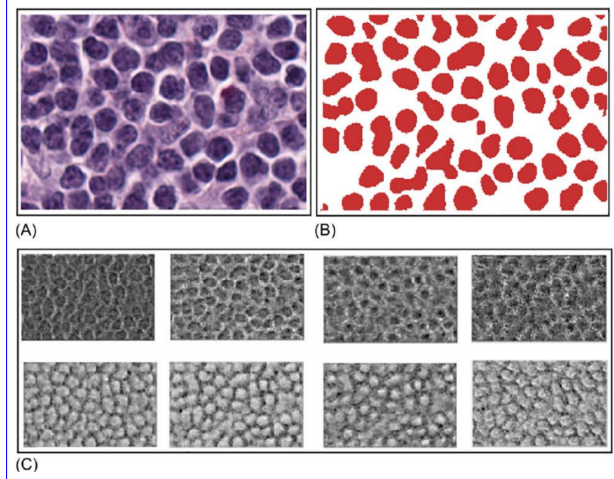


Figure 1.9: (A) An extract from an histological samples, used as input image for the model. (B) The exact segmentation mask. (C) Example of accentuated features during the training: (1-4) for back-ground recognition, (5-8) for nuclei detection. From [2].

551 the whole image. Instance segmentation extends semantic segmentation scope further
 552 by detecting and delineating each object of interest in the image (e.g. partitioning of
 553 individual nuclei in a histological image).

554 There are many prominent Neural Network architectures used in the computer vision
 555 community nowadays, based on very different ideas such as convolution, recursion,
 556 dimensionality reduction, and image generation. This section will provide an overview of
 557 the state of the art of this technology and will dwell briefly on the details behind some
 558 of those innovative architectures.

559 Recurrent Neural Networks (RNNs) and the LSTM

560 The typical application for RNN is processing sequential data, as written text,
 561 speech or video clips, or any other kind of time-series signal. In this kind of
 562 data, there is a strong dependency between values at a given time/position and
 563 values previously processed. Those models try to implement the concept of *memory*
 564 weaving connections, outside the main information flow of the network, with the
 565 previous NN's input. At each time-stamp, the model collects the input from the
 566 current time X_i and the hidden state from the previous step h_{i-1} and outputs a
 567 target value and a new hidden state (Figure 1.10). Typically RNN cannot manage
 568 easily long-term dependencies in long sequences of signals. There is no theoretical
 569 limitation in this direction, but often it arises vanishing (or exploding) gradient
 570 problematics during the training phase. A specific type of RNN has been designed
 571 to avoid this situation, the so-called Long Short Term Memory (LSTM) [19]. The

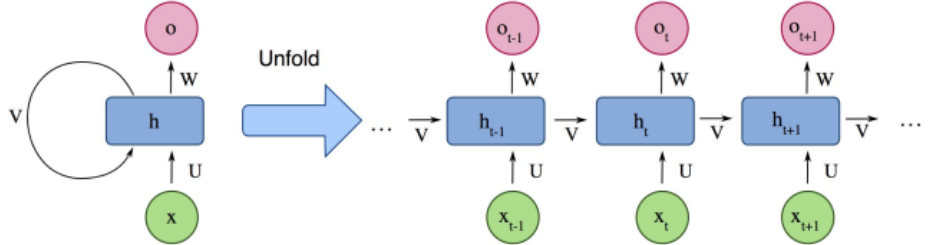


Figure 1.10: Example of the structure of a simple Recurrent Neural Network from [27].

572 LSTM architecture includes three gates (input gate, output gate, forget gate),
 573 which regulate the flow of information into and out from a memory cell, which
 574 stores values over arbitrary time intervals.

575 Encoder-Decoder and Auto-Encoder Models

576 Encoder-Decoder models try to learn the relation between an input and the corre-
 577 sponding output with a two steps process. The first step is the so-called *encoding*
 578 process, in which the input x is compressed in what is called the *latent-space* rep-
 579 resentation $z = f(x)$. The second step is the *decoding* process, where the NN
 580 predicts the output starting from the latent-space representation $y = g(z)$. The
 581 idea underneath this approach is to capture in the latent-space representation the
 582 underlying semantic information of the input that is useful for predicting the out-
 583 put. ED models are widely used in image-to-image problems (where both input
 584 and output are images) and for sequential-data processing (like Natural Language
 585 Processing, NLP). In Figure 1.11 is shown a schematic representation of this ar-
 586 chitecture. Usually, these model follow a supervised training, trying to reduce the
 587 reconstruction loss between the predicted output and the ground-truth output pro-
 588 vided while training. Typical applications for this technology are image-enhancing
 589 techniques like de-noising or super-resolution, where the output image is an im-
 590 proved version of the input image. Or image generation problems (e.g. plausible
 591 new human faces generation) in which all the properties which define the type of
 592 image under analysis should be learned in the representation latent space.

Generative Adversarial Networks (GANs)

The peculiarity of Generative Adversarial Network (GAN) lies in its structure. It is actually made of two distinct and independent modules: a generator and a discriminator, as shown in Figure 1.12. The first module G , responsible for the generation, typically learns to map a prior random distribution of input z to a target distribution y , as similar as possible to the target $G = z \rightarrow y$ (i.e. almost

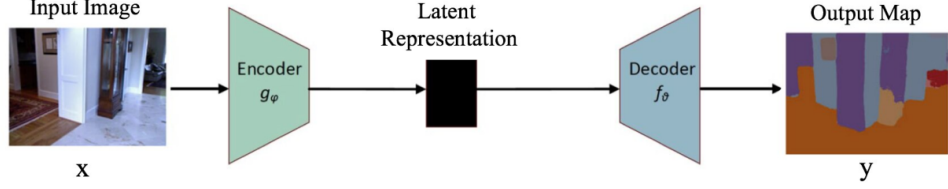


Figure 1.11: Example of the structure of a simple Encoder-Decoder Neural Network from [27].

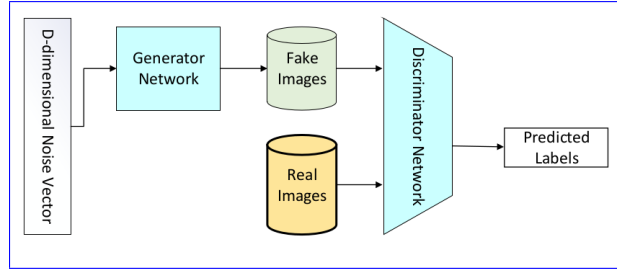


Figure 1.12: Schematical representation of a Generative Adversarial Networks, form [27].

any kind of image-to-image problem could be addressed with GANs, as in [20]). The second module, the discriminator D , instead is trained to distinguish between *real* and *fake* images of the target category. These two networks are trained alternately in the same training process. The generator tries to fool the discriminator and vice versa. The name adversarial is actually due to this *competition* within different parts of the network. The formal manner to set up this adversarial training lies in the accurate choice of a suitable loss function, that will look like:

$$L_{GAN} = \mathbb{E}_{x \sim p_{data}(x)}[\log D(x)] + \mathbb{E}_{z \sim p_z(z)}[\log(1 - D(G(z)))]$$

. The GAN is thus based on a min-max game between G and D . D aims to reduce the classification error in distinguishing fake samples from real ones, and as a consequence maximizing the L_{GAN} . On the other hand, G wants to maximize the D 's error, hence minimizing L_{GAN} . The result of the training process is the trained generator G^* , capable of produce an arbitrary number of new data (images, text, or whatever else):

$$G^* = \arg \min_G \max_D L_{GAN}$$

. This peculiar architecture has yielded several interesting results and it has been developed in many different directions, with influences and contaminations with other architectures [20].

593
594
595

596 **Convolutional Neural Networks (CNNs)**

597 As stated before CNNs are a staple choice in image processing DL applications.
598 They mainly consist of three types of layers:

- 599 i convolutional layers, where a kernel window of parameters is convolved with
600 the image pixels and produce numerical features maps.
- 601 ii nonlinear layers, which apply an activation function on feature maps (usually
602 element-wise). This step allows the network to introduce non-linear behavior
603 and then increasing its modeling capabilities.
- 604 iii pooling layers, which replace a small neighborhood of a feature map with some
605 statistical information (mean, max, etc.) about the neighborhood and reduce
606 the spatial resolution.

607 Given the arrangement of successive layers, each unit receives weighted inputs from
608 a small neighborhood, known as the receptive field, of units in the previous layer.
609 The stack of layers allows the NN to perceive different resolutions: the higher-
610 level layers learn features from increasingly wider receptive fields. The leading
611 computational advantage given by CNN architecture lies in the sharing of kernels'
612 weights within a convolutional layer. The result is a significantly smaller number
613 of parameters than fully-connected neural networks. In section 2.7 will be shown a
614 particular application of this architecture, known as *style-transfer* network, which
615 is a particular algorithm capable of implanting the visual texture of a *style* image
616 onto the content of a different image, producing interesting hybrid images. Some
617 of the most notorious CNN architectures include: AlexNet [23], VGGNet [40], and
618 U-Net [34].

619 For this work, U-net architecture is particularly interesting. The U-net model was
620 initially developed for biomedical image segmentation, and in its structure reflects char-
621 acteristics of both CNN and Encoder-Decoder models. Ronneberger et al.[34] proposed
622 this model for segmenting biological microscopy images in 2015. The U-Net architecture
623 is made of two branches, a contracting path to capture context, and a symmetric expand-
624 ing path (see Figure 1.13). The down-sampling flow is made of a Fully Convolutional
625 Network (FCN)-like architecture that computes features with 3×3 kernel convolutions.
626 On the other hand, the up-sampling branch exploits up-convolution operations (or de-
627 convolution), reducing the number of feature maps while increasing their dimensions.
628 Another characteristic of this architecture is the presence of direct connections between
629 layers of a similar level of compression in compressing and decompressing branches.
630 Those links allow the NN to preserve spatial and pattern information. The Network
631 flow eventually ends with a 1×1 convolution layer responsible for the generation of the
632 segmentation mask of the input image.

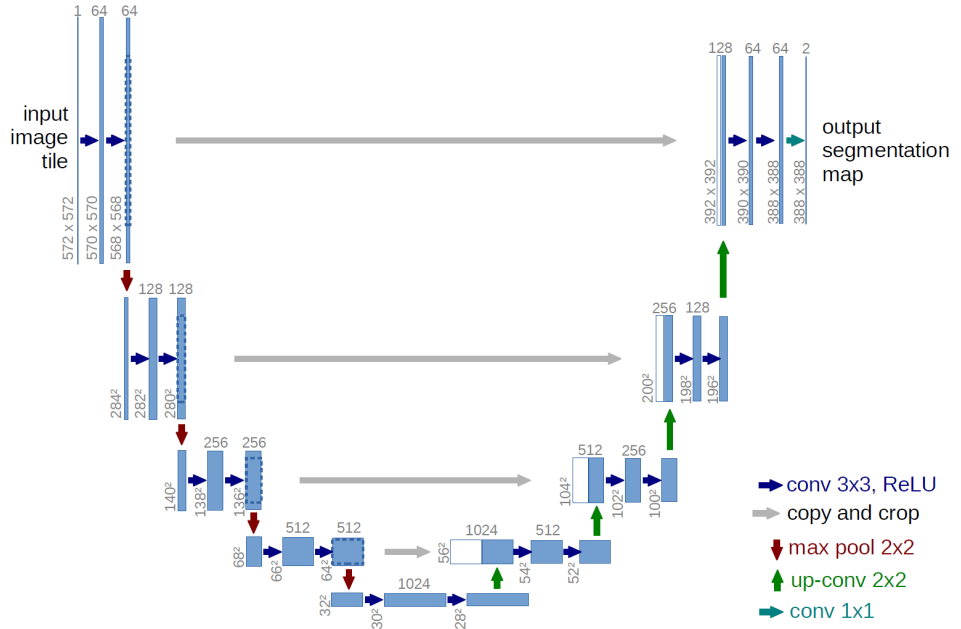


Figure 1.13: Scheme of the typical architecture of a U-net NN. This particular model was firstly proposed by Ronneberger et al. in [34].

A recent example of a practical application of a CNN to histological images could be found in [28]. In this work the `Inception v3` is trained on hand-labeled samples of pancreatic tissue (like in Figure 1) to recognise tumoral regions from healthy ones in a pancreatic tissue specimen treated with Ki67 staining. The `Inception v3` [33] network is a deep convolutional network developed by Google, trained for object detection and image classification on the ImageNet dataset [15]. Recognition of tumoral region of Ki67 stained pancreatic tissue samples is based on the detection and counting of some specific marker cells. In Figure 1.14 is shown a pair of original image and the computed segmentation mask, which label in red tumoral regions and in green the healthy ones. This work is based on a technique called `transfer learning`, which consists in the customization and specialization of a pre-trained NN previously trained for similar, but essentially different, tasks. The final part of the training of this version of `Inception v3` has been performed of a dataset of 33 whole slide images of Ki67 stained neuroendocrine tumor biopsies acquired from 33 different patients, digitized with a $20\times$ magnification factor and successively divided in 64×64 patches.

648 1.3.2 Image Segmentation Datasets

⁶⁴⁹ Besides the choice of suitable architecture the most important aspect while developing
⁶⁵⁰ a NN is the dataset on which perform the training process. Let's confine the discussion

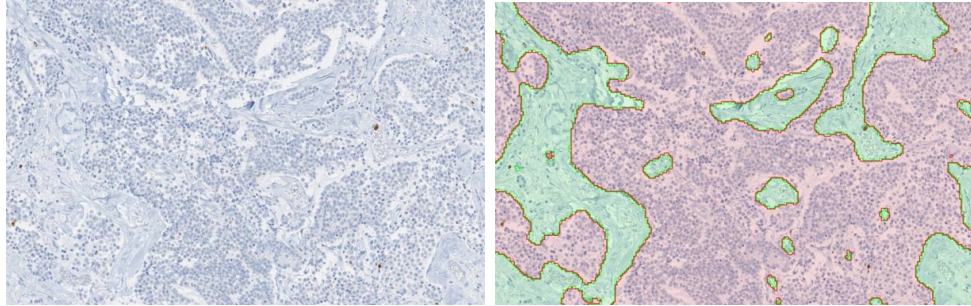


Figure 1.14: (left) Original image of a Ki67 stained pancreatic tissue sample, (right) the corresponding segmentation mask, which label in red tumoral regions and in green the healthy ones. From [28].

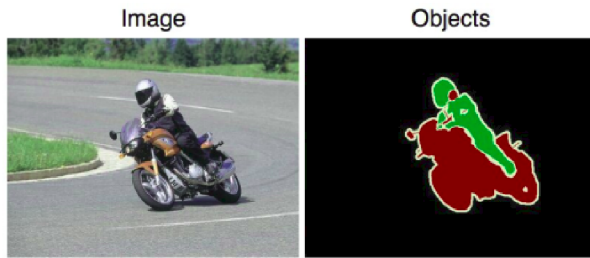


Figure 1.15: An example image from the PASCAL dataset and its corresponding segmentation mask [17].

651 only to image-to-image problems, like segmentation problems. There are a lot of widely
 652 used datasets, but I want to mention just a few of them to give the idea of their typical
 653 characteristics.

654 A good example of segmentation is the Cityscapes dataset [12], which is a large-scale
 655 database with a focus on semantic understanding of urban street scenes. The dataset
 656 is made of video sequences from the point of view of a car in the road traffic, from 50
 657 different cities in the world. The clips are made of 5K frames, labeled with extremely high
 658 quality at pixel-level and an additional set of 20K weakly-annotated frames. Each pixel
 659 in the segmentation mask contains the semantic classification, among over 30 classes of
 660 objects. An example of an image from this dataset is shown in Figure 1.7.

661 The PASCAL Visual Object Classes (VOC) [17] is another of the most popular
 662 datasets in computer vision. This dataset is designed to support the training of algo-
 663 rithms for 5 different tasks: segmentation, classification, detection, person layout, and
 664 action recognition. In particular, for segmentation, there are over 20 classes of labeled
 665 objects (e.g. planes, bus, car, sofa, TV, dogs, person, etc.). The dataset comes divided
 666 into two portions: training and validation, with 1,464 and 1,449 images, respectively. In
 667 Figure 1.15 is shown an example of an image and its corresponding segmentation mask.

668 As last mention I would report t he ImageNet project [15], which is a large visual
669 database designed for use in visual object recognition software research. It consists
670 of more than 14 million images have been hand-annotated by the project to indicate
671 what objects are pictured and in at least one million of the images, bounding boxes
672 are also provided. ImageNet contains more than 20,000 categories of objects. Since
673 2010, the ImageNet project runs an annual software contest, the ImageNet Large Scale
674 Visual Recognition Challenge (ILSVRC), where software programs compete to correctly
675 classify and detect objects and scenes. This kind of competitions is very important
676 for the research field, as it inspire and encourage the development of new models and
677 architectures.

678 It is worth mentioning that in the medical image processing domain typically the
679 available dataset is definitely not that rich and vast (that is actually the seed of this
680 work) and thus many techniques of data augmentation have been devised, to get the
681 best out of the restricted amount of material. Generally, data augmentation manipu-
682 lates the starting material applying a set of transformation to create new material, like
683 rotation, reflection, scaling, cropping and shifting, etc. Data augmentation has been
684 proven to improve the efficacy of the training, making the model less prone to over-
685 fitting, increasing the generalization power of the model, and helping the convergence to
686 a stable solution during the training process.

₆₈₇ **Chapter 2**

₆₈₈ **Technical Tools for Model
₆₈₉ Development**

₆₉₀ As mentioned in the introduction, this project wants to produce synthetic histological
₆₉₁ images paired with their corresponding segmentation mask, to train Neural Networks
₆₉₂ for the automatization of real histological images analysis. The production of artificial
₆₉₃ images passes through the processing of a three dimensional, virtual model of a his-
₆₉₄ tological structure, which is the heart of this thesis work. The detailed description of
₆₉₅ the development of the two proposed histological models will follow the present chapter
₆₉₆ and will occupy all the chapter 3. Here I will dwell, instead, on every less common
₆₉₇ tool employed during the models' designing phase. From the practical point of view, this
₆₉₈ project is quite articulated and the development has required the harmonization of many
₆₉₉ different technologies, tools, and code libraries. The current chapter should be seen as a
₇₀₀ theoretical complement for chapter 3, and its reading is suggested to the reader for any
₇₀₁ theoretical gap or for any further technical deepening. The reader already familiar with
₇₀₂ those technical tools should freely jump to the models' description.

₇₀₃ All the code necessary for the work has been written in a pure Python environment,
₇₀₄ using several already established libraries and writing by my self the missing code ~~for~~
₇₀₅ some specific applications. I decided to code in Python given the thriving variety of
₇₀₆ available libraries geared toward scientific computation, image processing, data analysis,
₇₀₇ and last but not least for its ease of use (compared to other programming languages). In
₇₀₈ each one of the following subsections ~~will be mentioned~~ I will mention the specific code
₇₀₉ libraries which have been employed in this project for every technical necessity.

₇₁₀ **2.1 Quaternions**

₇₁₁ Quaternions are, in mathematics, a number system that expands to four dimensions the
₇₁₂ complex numbers. They have been described for the first time by the famous mathemati-

⁷¹³ cian William Rowan Hamilton in 1843. This number system define three independent
⁷¹⁴ *imaginary* units $\mathbf{i}, \mathbf{j}, \mathbf{k}$ as in (2.1), which allows the general representation of a quaternion
⁷¹⁵ \mathbf{q} is (2.2) and its inverse \mathbf{q}^{-1} (2.3) where a, b, c, d are real numbers:

$$\mathbf{i}^2 = \mathbf{j}^2 = \mathbf{k}^2 = \mathbf{ijk} = -1, \quad (2.1)$$

$$\mathbf{q} = a + bi + cj + dk, \quad (2.2)$$

$$\mathbf{q}^{-1} = (a + bi + cj + dk)^{-1} = \frac{1}{a^2 + b^2 + c^2 + d^2} (a - bi - cj - dk). \quad (2.3)$$

⁷¹⁶ Furthermore, the multiplication operation between quaternionn does not benefit from
⁷¹⁷ commutativity, hence the product between basis elements will behave as follows:

$$\begin{aligned} \mathbf{i} \cdot 1 &= 1 \cdot \mathbf{i} = \mathbf{i}, & \mathbf{j} \cdot 1 &= 1 \cdot \mathbf{j} = \mathbf{j}, & \mathbf{k} \cdot 1 &= 1 \cdot \mathbf{k} = \mathbf{k} \\ \mathbf{i} \cdot \mathbf{j} &= \mathbf{k}, & \mathbf{j} \cdot \mathbf{i} &= -\mathbf{k} \\ \mathbf{k} \cdot \mathbf{i} &= \mathbf{j}, & \mathbf{i} \cdot \mathbf{k} &= -\mathbf{j} \\ \mathbf{j} \cdot \mathbf{k} &= \mathbf{i}, & \mathbf{k} \cdot \mathbf{j} &= -\mathbf{i}. \end{aligned} \quad (2.4)$$

⁷¹⁸ This number system has plenty of peculiar properties and applications, but for this
⁷¹⁹ project, quaternions are important for their ability to represent, in a very convenient way,
⁷²⁰ rotations in three dimensions. The particular subset of quaternions with vanishing real
⁷²¹ part ($a = 0$) has a useful, yet redundant, correspondence with the group of rotations in
⁷²² tridimensional space $\text{SO}(3)$. Every 3D rotation of an object can be represented by a 3D
⁷²³ vector \vec{u} : the vector's direction indicates the axis of rotation and the vector magnitude $|\vec{u}|$
⁷²⁴ express the angular extent of rotation. However, the matrix operation which expresses
⁷²⁵ the rotation around an arbitrary vector \vec{u} it is quite complex and does not scale easily
⁷²⁶ for multiple rotations [7], which brings to very heavy and entangled computations.

⁷²⁷ Using quaternions for expressing rotations in space, instead, it is very convinient.
⁷²⁸ Given the unit rotation vector \vec{u} and the rotation angle θ , the corresponding rotation
⁷²⁹ quaternion \mathbf{q} becomes (2.6):

$$\vec{u} = (u_x, u_y, u_z) = u_x \mathbf{i} + u_y \mathbf{j} + u_z \mathbf{k}, \quad (2.5)$$

$$\mathbf{q} = e^{\frac{\theta}{2}(u_x \mathbf{i} + u_y \mathbf{j} + u_z \mathbf{k})} = \cos \frac{\theta}{2} + (u_x \mathbf{i} + u_y \mathbf{j} + u_z \mathbf{k}) \sin \frac{\theta}{2}, \quad (2.6)$$

$$\mathbf{q}^{-1} = \cos \frac{\theta}{2} - (u_x \mathbf{i} + u_y \mathbf{j} + u_z \mathbf{k}) \sin \frac{\theta}{2}, \quad (2.7)$$

⁷³⁰ where in (2.6) we can clearly see a generalization of the Euler's formula for the
⁷³¹ exponential notation of complex numbers, which hold for quaternions. It can be shown

732 that the application of the rotation represented by \mathbf{q} on an arbitrary 3D vector \vec{v} should
733 be easily expressed as:

$$\vec{v}' = \mathbf{q}\vec{v}\mathbf{q}^{-1}, \quad (2.8)$$

734 using the Hamilton product defined on quaternions (2.4). This rule raises a very con-
735 vinient and an extremily scalable way to compute consecutive rotations in space. Given
736 two independent and consecutive rotations represented by the two quaternions \mathbf{q} and \mathbf{p}
737 applied on the vector \vec{v} the resulting rotated vector \vec{v}' is simply yielded as:

$$\vec{v}' = \mathbf{p}(\mathbf{q}\vec{v}\mathbf{q}^{-1})\mathbf{p}^{-1} = (\mathbf{pq})\vec{v}(\mathbf{qp})^{-1}, \quad (2.9)$$

738 which essentially is the application of the rotation $\mathbf{r} = \mathbf{qp}$ on the vector \vec{v} . This repre-
739 sentation is completely coherent with the algebra of 3D rotations, which does not benefit
740 from commutativity in turn.

741 Given this property, quaternions are indeed widely used in all sorts of applications
742 of digital 3D space design, as for simulations and videogame. The position of an object
743 in the space in simulations is generally given by the application of several independent
744 rotations, typically in the order of a tenth of rotations, which with quaternions is given
745 easily by the product of simple objects. Every other alternative method would imply the
746 use of matrix representation of rotations or other rotation systems as Euler's angles and
747 would eventually make the computation prohibitive.

748 The use of quaternions in this work will be justified in section 3.1, while speaking of
749 parametric L-systems in 3D space, used to build the backbone of the ramified structure
750 of blood vessels in the reconstruction of a sample of pancreatic tissue.

751 I was able to find many Python libraries for computation with quaternions, but the
752 one I appreciated the most for its interface and ease of use was the `pyquaternion`. With
753 this library, it's immediate the definition of a quaternion by its correspondent rotation
754 vector, and the multiplication between quaternions is straightforward.

755 2.2 Parametric L-Systems

756 Lindenmayer systems, or simply L-systems, were conceived as a mathematical theory of
757 plant development [25] in 1968 by Aristid Lindenmayer. Successively, a lot of geometri-
758 cal interpretations of L-systems were proposed to make them a versatile instrument for
759 modeling the morphology typical of plants and other organic structures. As a biologist,
760 Lindenmayer studied different species of yeast and fungi and worked the growth patterns
761 of various types of bacteria (e.g. as the *cyanobacteria Anabaena catenula*). The main
762 purpose for which L-systems were devised was to allow a formal description of the devel-
763 opment of simple multicellular living organisms. Subsequently, the potentiality of these
764 systems was expanded to describe higher-order plants and complex branching structures.

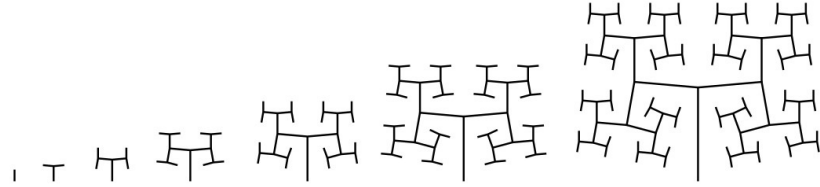


Figure 2.1: Growth pattern for the space-filling fractal-like system, used to mimic the blood vessel bifurcations in sec 3.1.

765 An L-system is in general defined by an *axiom* sequence and some development *rules*,
 766 which are recursively applied to the sequence and lead its development. The original
 767 proposed L-system was fairly simple and shows really well the idea underneath:

$$\begin{aligned} \textit{axiom} &: A \\ \textit{rules} &: (A \rightarrow AB), \quad (B \rightarrow A) \end{aligned}$$

768 where A and B could be any two different patterns in the morphology of an algae, or
 769 could be different bifurcations in a ramified structure. The iterative application of the
 770 rules to the axiom sequence, let's say for 7 times, will produce the following sequence:

$$\begin{aligned} n = 0 & : A \\ n = 1 & : AB \\ n = 2 & : ABA \\ n = 3 & : ABAAB \\ n = 4 & : ABAABABA \\ n = 5 & : ABAABABAABAAB \\ n = 6 & : ABAABABAABAABABAABABA \\ n = 7 & : ABAABABAABAABABAABAABABAABAAB . \end{aligned}$$

771 This kind of tool, as will be shown also in 3.1, is particularly suited for the creation of
 772 structures with fractal behavior, and it has been used in this work to create the backbone
 773 of the entangled bifurcation in blood vessels in the modelization of pancreatic tissue. In
 774 particular, there was the need for a fractal-like space-filling ramification as the one shown
 775 in Figures 2.1.

776 The system in Figure 2.1 represent the successive ramification of a structure which
 777 grows adding segments gradually shorter, by a lenght ratio parameter R and inclined
 778 of $\delta = \pm 85^\circ$ respect the previous branch. The axiom and the rules that produce this
 779 structure are the following:

$$\begin{aligned}
& axiom : A & (2.10) \\
& rule_1 : A \rightarrow F(1)[+A][-A] \\
& rule_2 : F(s) \rightarrow F(s \cdot R)
\end{aligned}$$

780 where A represent the start of a new branch and $F(s)$ represent a branch of lenght s .
781 The presence of a rule which acts differently depending on the target object, is an further
782 sophistication respect to the standard L-system. For this reason these systems are called
783 *parametric* L-systems.

784 The use of standard L-systems turned out to be widespread, and there were a lot of
785 different Python libraries at my disposal for coding. By the way, parametric L-systems
786 were not just as popular, and I was not able to find a reliable library on which to build
787 my work. I decided then to code a parametric branching system able to recreate the
788 structure with rules (2.10) at any desired level of iteration. Having created the tool I
789 needed on my own I was able to add all the optional features I would have needed during
790 the development, like an adjustable degree of angular noise in the branch generation.

791 2.3 Voronoi Tassellation

792 Voronoi diagrams, or Voronoi decompositions, are space-partitioning systems, which
793 divides an n -dimensional Euclidian space into sub-regions depending on the proximity
794 to a given set of objects. More precisely, given an n -dimensional space and m starting
795 point p_1, \dots, p_m inside it, the whole space will be subdivided in m adjacent regions. Every
796 point of the space is assigned to the region correspondent to the nearest starting point.
797 In Figure 2.2 is shown a practical example of a Voronoi decomposition of a plane into
798 20 regions corresponding to the 20 starting points. Informal use of Voronoi diagrams
799 can be traced back to Descartes in 1644, and many other mathematicians after him.
800 But, Voronoi diagrams are named after Georgy Feodosievych Voronoy who defined and
801 studied the general n-dimensional case in 1908 [46].

802 More precisely, let X be a metric space and d the distance defined on it. Let K be
803 the set of indices and let $(P_k)_{k \in K}$ be the tuple of sites in the space X . The k^{th} Voronoi
804 cell R_k , associated with the site P_k is the set of all the points in X whose distance to P_k
805 is smaller than the distance to any other site P_j , with $j \neq k$, or in other words:

$$R_k = \{x \in X \mid d(x, P_k) \leq d(x, P_j) \forall j \in K, j \neq k\}, \quad (2.11)$$

806 depending on the notion of distance defined on the space X the final redistribution in
807 subregions will look very differently.

808 In addition to the choice of the distance function, another fundamental factor is the
809 distribution of sites in the space to be divided. If the points are chosen equally and ho-
810 mogenously distributed the final distribution will appear as a simple regular lattice, while

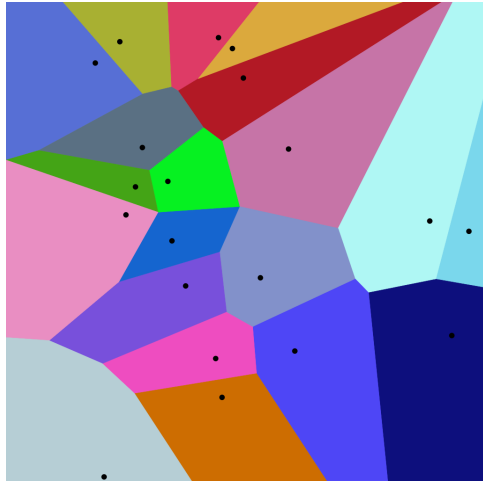


Figure 2.2: Example of a Voronoi decomposition of a plane into 20 regions corresponding to 20 starting points.

811 a completely random distribution of points in the space will provide a decomposition in
 812 cells with very different shapes and volumes, as shown in Figure 2.3. Interesting results
 813 concerning points from a semi-random distribution will be shown in section 3.1, which
 814 leads to decomposition with a good richness in shapes but with the desired homogeneity
 815 in volumes.

816 The Voronoi decomposition has been of great interest in this project for the division
 817 of a 3D space in subregions, to recreate the spatial distribution of cells in a sample of
 818 human tissue, as will be shown in section 3.1. The formal definition of Voronoi regions
 819 (2.11) ensures the convexity of each decomposition's tassel, which in three-dimensional
 820 space would be adjacent convex polyhedrons. Every tassel of the decomposition will
 821 be represented by a bounded 3-dimensional convex hull¹, with except for those most
 822 external cells which are unbounded and requires special attention while using.

823 The most widespread tool for the computation of Voronoi decompositions in Python
 824 is contained in the `spatial` submodule of the famous library `SciPy` [45], which is a staple
 825 tool for an incredible variety of scientific algorithms. The `Voronoi` object from `Scipy`
 826 library offers a very efficient algorithm for space-partitioning, and it has been one of the
 827 pillars for the modelization of tissues. Unluckily this module does not easily allow to
 828 perform Voronoi decomposition with different definitions of distance functions d other
 829 than the Euclidian distance, which would have allowed interesting studies.

¹See section 2.5 for further details.

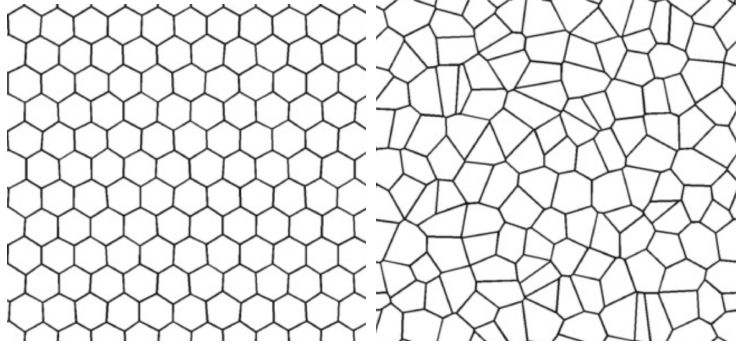


Figure 2.3: On the right an example of 2D Voronoi decomposition resulting from homogeneously distributed points in the plane. On the left the resulting decomposition obtained from randomly distributed points in the plane, from [3].

830 2.4 Saltelli Algorithm - Random Number Generation

831 As mentioned in section 2.3, in this project there was the need for quasi-random number
 832 generation for the production of Voronoi tessellations. Quasi-random sequences (or low-
 833 discrepancy sequences) are patterns of numbers that emulate the behavior of uniform
 834 random distributions but have a more homogeneous and quick coverage of the sampling
 835 domain, which provides an important advantage in applications as in quasi-Monte Carlo
 836 integration techniques, as shown in Figure 2.4. In computer science there is not any
 837 possibility of recreating *true* random sequences, hence any stochasticity is completely
 838 deterministic in its essence even if produced by very chaotic processes². Indeed, every
 839 algorithm for random number generation is completely repeatable given its starting sta-
 840 tus. Quasi-random sequences are completely deterministic too, but implements more
 841 *regular*, well-behaved algorithms.

842 A first good example to understand the concept of quasi-random generation could be
 843 an additive recurrence, as the following:

$$s_{n+1} = (s_n + \alpha) \bmod 1, \quad (2.12)$$

844 which for every seed element s_0 and real parameter α produced completely different
 845 sequences.

846 In the bottom line of Figure 2.4 is clearly visible the good and homogeneous coverage
 847 of the sampling domain, although it is strongly visible a regular pattern between points,
 848 which does not convey an *organic* sensation at all. However, increasing the complexity of

²A chaotic process is a deterministic process which has an extremely sensible dependence on its starting conditions. This property mimics very effectively the behavior of true random processes, which are intrinsically forbidden in computer science.

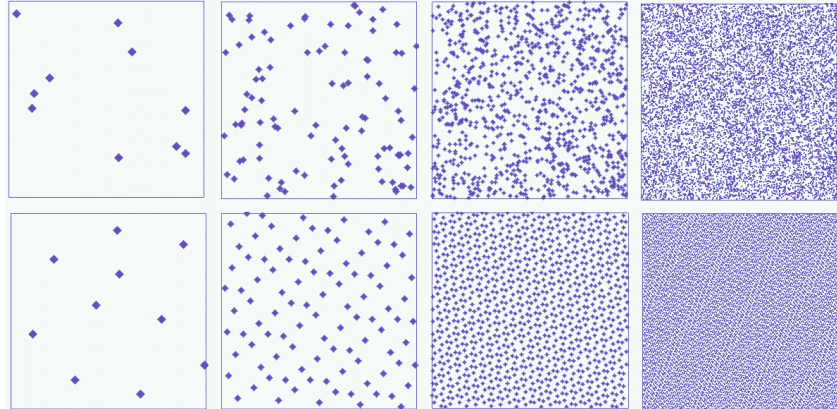


Figure 2.4: Coverage of the unit square with an additive quasirandom numbers sequence as in 2.12 (up) and for uniformly sampled random numbers (bottom). From left to right: 10, 100, 1000, 10000 points.

our very simple starting model 2.12 it is possible to overcome this *artificial* appearance of sampled points and to produce very good samples.

A notorious algorithm for quasi-random number generation is the Sobol sequence, introduced by the russian mathematician Ilya M. Sobol in 1967 [43]. In its work, Sobol wanted to construct a sequence x_n of points in the s -dimensional unitary hypercube $I^s = [0, 1]^s$ such as for any integrable function f :

$$\lim_{n \rightarrow \infty} \frac{1}{n} \sum_{i=1}^n f(x_i) = \int_{I_s} f. \quad (2.13)$$

Sobol wanted to minimize the *holes* in the sampled domain (which it could be shown to be a property that helps the convergence of the sequence) and minimize as well the *holes* in every lower-dimension projection of the sampled points. The particularly good distributions that fulfill those requirements are known as (t, m, s) -nets and (t, s) -sequences in base b .

To better understand them we need first to define the concept of s -interval in base b , which is a subset of I_s such as:

$$E_s^b = \prod_{j=1}^s \left[\frac{a_j}{b^{d_j}}, \frac{a_j + 1}{b^{d_j}} \right), \quad (2.14)$$

where a_j and d_j are non-negative integers, and $a_j < b^{d_j}$ for all j in $\{1, \dots, s\}$.

Let be t and m two integers such as $0 \leq t \leq m$. A (t, m, s) -net in base b is defined as a sequence x_n of b^m points of I_s such that:

$$\text{Card } \mathbf{P} \cap \{x_1, \dots, x_n\} = b^t \quad (2.15)$$

865 for all the elementary interval \mathbf{P} in base b of hypervolume $\lambda(\mathbf{P}) = b^{t-m}$.

866 Given a non-negative integer t , a (t, s) -sequence in base b is an infinite sequence of
867 points x_n such that for all integers $k \geq 0$, $m \geq t$ the sequence $\{x_{kb^m}, \dots, x_{(k+1)b^m-1}\}$ is
868 a (t, m, s) -net in base b .

869 Sobol in his article described in particular (t, m, s) -net and (t, s) -sequence in base 2.
870 A more thorough description of all the formal properties of those particular sequences
871 could be found in [42].

872 In order to perform the actual sampling during the modelization, it has been used the
873 `saltelli` module from the `SALib` library, which performs sampling in an s -dimensional
874 space following the Saltelli algorithm, which is a specific improved version of the Sobol
875 algorithms oriented toward the parameter sensitivity analysis [36], [37].

876 2.5 Planar Section of a Polyhedron

877 As will be shown in section 3.1 a fundamental step for the functioning of the modelization
878 is the planar section of a three-dimensional polyhedron. It turned out that there is
879 no general rule to perform a planar section of a convex polyhedron with an arbitrary
880 number of faces, respect to an arbitrary sectioning plane. Hence, I devised an algorithm
881 to handle this task. In the case of a full intersection, the result of the sectioning process
882 of a polyhedron is a polygonal surface, otherwise, it could be an empty set of points or
883 a segment in case of particular tangency, but those two cases are not of interest to the
884 model. This tool has been created from scratch by me in the preliminar design phase and
also the implemented algorithm has been devised by me and chosen as the best option
among other possibilities. It is not fruit of an extended and thorough formal analysis,
hence it has not the pretentious to be an extremely optimized algortihm. Nevertheless,
this tool passed all the test I required and yielded the expected results.

885 Given a convex polyhedron with n vertices and a sectioning plane p , let V be the set
886 of all the vertices and $f_p(\vec{x})$ the equation defining the plane. The algorithm is defined
887 by the following steps:

- 888 1. Divide V in two subsets: A made of those vertices which lie above and B , made of
those which lie below the sectioning plane. Like in 2.16:

$$A = \{\vec{v} \in V \mid f_p(\vec{v}) \geq 0\} \quad (2.16)$$
$$B = \{\vec{v} \in V \mid f_p(\vec{v}) \leq 0\}$$

889 If any of the two subsets turns out to be empty the plane p does not intersect the
890 polyhedron, and the section is empty. A and B are represented in different colors
891 in Figure 2.5.

- 892 2. Detect, and *draw*, any possible line that crosses two points respectively from A and
 B . If n_A and n_B are the numbers of points above and below the plane then there

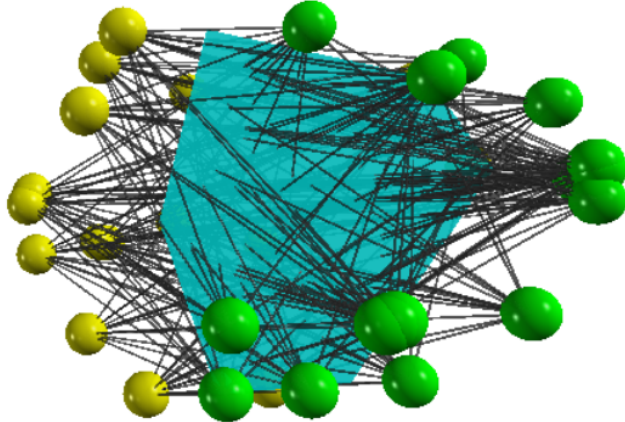


Figure 2.5: In this picture is shown an example of the application of the algorithm for the planar section on a polyhedron. The vertices are divided into two groups, with different colors yellow and green. All the possible lines between any couple of vertices picked from the two classes are drawn in dark gray. In Turquoise the resulting planar section, obtained as the convex hull containing all the intersections between the lines and the plane.

897 will be $n_A \times n_B$ possible lines. In Figure 2.5 all the lines between the two classes
 898 of points are drawn in dark gray.

- 899 3. Detect P , the set of all the points from the intersection between the $n_A \times n_B$ lines
 900 from the previous step and the sectioning plane p . All these points will lie on the
 901 same plane, within the boundaries of the polygonal section.
- 902 4. The final polygon is then yielded by computing the convex hull of the points in
 903 P . The convexity of the starting polyhedron in fact ensures the convexity of any
 904 section of the solid.

905 The result of the algorithm is, as just stated, a convex hull, which in geometry
 906 is defined as the smallest convex envelope or convex closure of a set of points. In 2
 907 dimensions is the smallest convex polygon containing a certain set of points in a plane
 908 (In Figure 2.6 is shown the so-called “rubber band effect”), and in 3 dimensions it is the
 909 smallest convex polyhedron containing a set of points in the space.

910 In Python, the most convenient way to work with convex hulls was to use the sub-
 911 module `spatial.ConvexHull` from the SciPy library [45]. This module allows also a
 912 convenient way for plotting images with Matplotlib, which is the point of reference for
 913 plotting and image formation in Python.

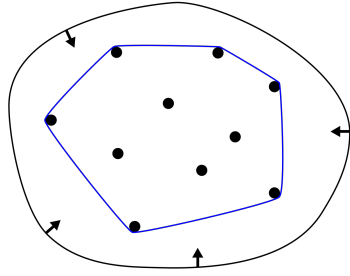


Figure 2.6: Representation of the convex hull of a bounded planar set of points. This particular enclosure goes under the name of "rubber band effect".

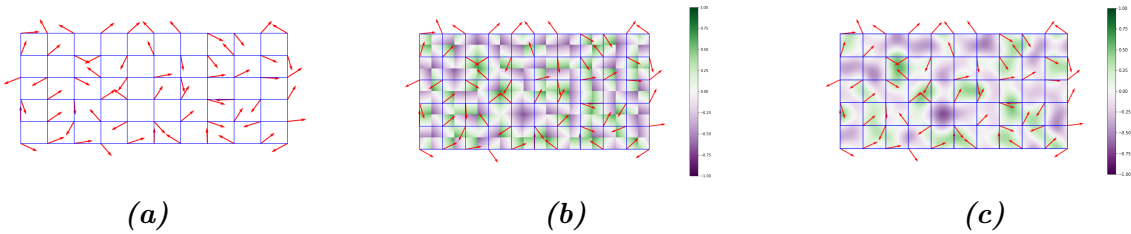


Figure 2.7: The three main steps of the algorithm to produce Perlin noise. In 2.7a the plane discretization and the assignment of a gradient vector to every node of the grid. In 2.7b the computation of the dot product with all the points inside the discretization and in 2.7c the interpolation of the values to create the final function.

914 2.6 Perlin Noise

915 Perlin noise is a widely used form of noise in computer graphics, which mimics very
 916 well natural and smooth fluctuations around a constant value. It has been developed by
 917 Ken Perlin in 1983, and it is now the staple tool for giving texture to object in virtual
 918 modelization, often considered the *salt* of computer graphics texturization. The Perlin
 919 noise is a gradient-based algorithm defined on grid discretization of a n -dimensional
 920 space. The algorithm involves three subsequent steps:

- 921 1. The first step is to discretize the n -dimensional space in a regular lattice: the
 922 dimension of the grid will impact heavily on the scale of the noise. As in Figure
 923 2.7a at every node of the grid is assigned a randomly oriented n -dimensional unitary
 924 gradient vector. This is the preliminary setup which will allow the computation of
 925 the actual noise function in every point of the space.
- 926 2. Given the candidate point \vec{x} between the grid nodes onto which evaluate the noise
 927 there are 2^n nearest grid nodes. For each one of these 2^n nodes, it is evaluated the

928 distance vector from \vec{x} as the offset between the two points. Then it is computed
929 the dot product between every pair made of nearby gradient vectors and the offset
930 vector. This operation should be thought of as made on every point in the lattice,
931 as in Figure 2.7b, where at every point of the grid is represented just one of the
932 $2^2 = 4$ series of dot products.

- 933 3. The final step is the interpolation between the 2^n series of dot products. To per-
934 form the interpolation usually is used a function with vanishing first degree (and
935 preferably also second degree) derivative in correspondence of the 2^n grid nodes ³.
936 This means that the noise function will pass through zero at every node and have
937 a gradient equal to the pre-computed grid node gradient. These properties give
938 Perlin noise its characteristic spatial scale and smoothness.

939 In general, the final result of the algorithm is a smooth function with a random-
940 like behavior that mimics really well an organic appearance, like in Figure 2.8, with
941 fluctuation around the value 0, with amplitude $\in [0; 1]$. The surface in Figure 2.8 has
942 been produced plotting in 3D the results of the function `pnoise2` from the library `noise`,
943 which offers a tool for the production of different type of noise. In order to put in practical
944 use this module some adjustment were required. The particular function `pnoise2` simply
945 yields the value of the Perlin noise surface in correspondence to a single (x, y) point in the
946 plane in a deterministic way. There was not the possibility to generate different whole
947 Perlin surfaces every run. To overcome this limitation I made a vectorized⁴ version of
948 `pnoise2` able to evaluate the function over an arbitrary wide grid of points expressed as
949 set of all the pairs of coordinates (x, y) of the grid's nodes. In this way a single call to
950 the function is able to produce the entire surface covering the grid, in the form of a single
951 NumPy 3D-array. Furthermore, to recover the possibility of generating always different
952 surfaces as in a random generation, I inserted an offset coordinate (x_O, y_O) , which moves
953 in the plane the origin of the surface generation. This pair of offset coordinates then acts
954 also as a *seed* in the generation, allowing to completely recreate previously generated
955 material in a controlled way.

956 2.7 Style-Transfer Neural Network

957 Style-Transfer Neural Networks are common models, able of creating new hybrid images
958 implanting the visual style from an image preserving the visual content of another image.

³Usually are used functions with a sigmoidal behavior, like any smoothstep function, which is a family of very common items in computer graphics.

⁴In Python the staple tool for scientific, number-cruncher computation is the NumPy library, which allows a fast, complete and efficient way to perform computation between number structure. The operation of transforming a function which acts on a single value (or pair of values) to a function able to perform on a suitable datastructure is called *vectorization*, and its the recomended way to proceed when handling numerical functions in Python.

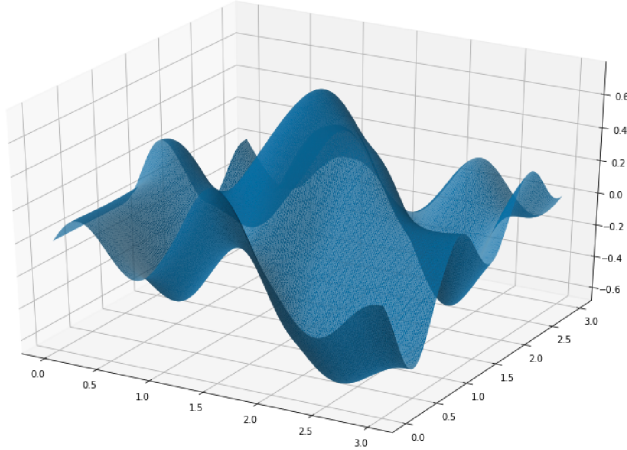


Figure 2.8: Example of Perlin noise 2D function produced while working on this project. This surface offers a smooth variation around the value 0 with amplitudes $\in [0; 1]$.

959 The two images necessary for the algorithm are called *style* image S and *content* image
 960 C , and the resulting *styled* picture X , as in Figure 2.9.

961 There are many different tested and comparable architectures to compute this kind
 962 of algorithm. In my work I decided to use in particular the procedure described in [18],
 963 using the PyTorch ecosystem to implement the necessary code.

964 The backbone of the architecture is the VGG-19 network, which is a convolutional
 965 neural network 19 layers deep, as in Figure 2.10. This huge model has been pre-trained
 966 on over a million images from the ImageNet database [16], for the classification into
 967 over than 1000 classes of objects. As a result, the network has learned rich feature
 968 representations for a wide range of images. The best (and conceptually the only) way to
 969 load a pre-trained model is to load the ordered set of weights that define the network and
 970 to initialize an empty module with those values. This is the perfect start for creating a
 971 style transfer network, which requires a further and briefer training phase, to completely
 972 customize the network.

973 The key ingredient for finalizing the model is to insert some little but fundamental
 974 modifications and to extend the training on the pair of input images. This final training
 975 should be aware of the *concepts* of the visual style and visual content of the image, and
 976 the operation should try to preserve them both. This is usually done minimizing two
 977 new loss function, computed between the staring image and the produced image:

978 Content Loss

979 The content loss is a function that represents a weighted version of the content
 980 distance for an individual layer. The most commonly used function to evaluate the
 981 preservation of content between two images is the simple Mean Squared Error as



Figure 2.9: Different examples of application of a style-transfer NN on the same content image, with different style images, from [18]. The original picture depicts the Neckarfront in Tbingen, Germany (TOP-LEFT). The painting used as style image shown in the bottom left corner of each panel are in clockwise order: • The Shipwreck of the Minotaur by J.M.W. Turner, 1805 • Femme nue assise by Pablo Picasso, 1910 • Composition VII by Wassily Kandinsky, 1913 • Der Schrei by Edvard Munch, 1893 • The Starry Night by Vincent van Gogh, 1889.

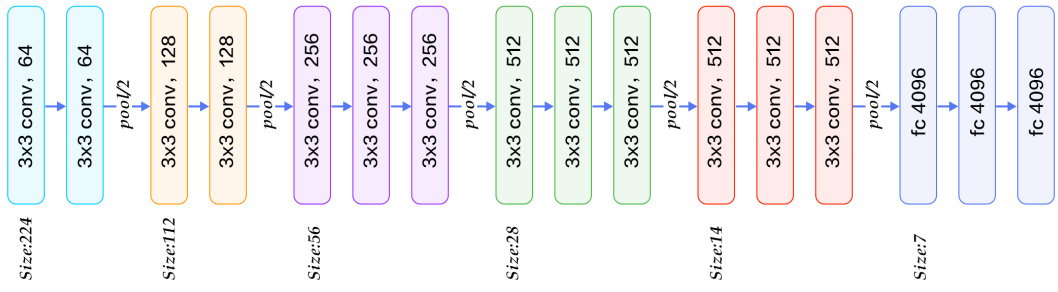


Figure 2.10: The structure of the VGG 19 network. It is for its most convolutional NN with 224×224 input size and with some downsampling layers which reduce the first two dimensions of the tensors along with the information flux of the network. At the very end of the architecture, there are three subsequent fully connected layers, responsible for the actual classification based on the features extracted from the previous layers.

982 in equation (1.5). It can be computed between any couple of same-sized object,
 983 hence also between the results of the same feature maps on the images X and C
 984 at the same layer L :

$$L_{Cont} = \|F_{XL}F_{CL}\|^2. \quad (2.17)$$

985 In order to evaluate this content loss, it is necessary to insert a custom transparent⁵
 986 layer directly after the convolution layer(s) that are being used to compute the
 987 content distance.

988 Style Loss

989 The concept of *style* loss function is the true novelty introduced by [18]. This loss
 990 function is implemented similarly to the content loss module, as it will act as a
 991 transparent layer in the network. The computation of the style loss requires in
 992 advanced the evaluation of the Gram matrix G_{XL} at a certain layer L . A Gram
 993 matrix is a result of multiplying a given matrix by its transposed matrix. In this
 994 case, the matrix to multiplicate is a reshaped version of the feature maps F_{XL} :
 995 \hat{F}_{XL} , a $K \times N$ matrix, where K is the number of feature maps at layer L and N
 996 is the length of any vectorized feature map F_{XL}^k . Furthermore, the Gram matrix
 997 must be normalized by dividing each element by the total number of elements in the
 998 matrix. The style distance is now computed using the mean square error between
 999 G_{XL} and G_{SL} :

$$L_{Style} = \|G_{XL}G_{SL}\|^2. \quad (2.18)$$

1000 After the appropriate insertion of the loss-function evaluator layers, one last piece for
 1001 finalizing the model is the right choice of the gradient descent optimizer. As in [18] and
 1002 according to the Deep Learning community the optimizer which suite best this role is the
 1003 Limited Memory-BFGS [8],[39]. L-BFGS is an iterative algorithm in the family of quasi-
 1004 Newton methods that approximates the Broyden-Fletcher-Goldfarb-Shanno algorithm
 1005 (BFGS) using a limited amount of computer memory, and it is a popular choice when
 1006 estimating parameters of a non-linear differentiable scalar function.

1007 The final phase of the training process thus makes run the optimizer for hundreds of
 1008 epochs on X , C , and S , and reduce the two loss functions values acting on the network's
 1009 parameters. After the fine-tuning of the weights, the hybrid image is produced, as in
 1010 Figure 2.9.

1011 2.8 Working Environment

1012 In this section I will briefly describe the machine I used to develop my project and the
 1013 working environment I built. All the work has been done on my personal computer,

⁵A transparent layer is a layer that performs some operations, like evaluating a function on its input, but returns as output an unchanged copy of its input.

1014 mounting a `GNU/linux` operating system, in particular 18.04 LTS `Ubuntu` version. The
1015 computer mounts an Intel i7 core, 8 Gb of RAM beside an 2Gb NVidia 940MX GPU.
1016 All the Python libraries have been installed and harmonized in a virtual environment
1017 mounting `Python 3.7.6`. All the code produced during the development, the images,
1018 and the data produced have been collected in a devoted repository on GitHub [14], which
1019 is freely available.

1020 As a conclusion for this chapter I will re-collect all the references to the different
1021 `Python` libraries I used during the development of this work:

1022 **NumPy:** NumPy is the pillar of every scientific computation-oriented library. Is the most
1023 spread library for heavy multidimensional numerical computation, and it offers a
1024 broad variety of tools like random number generators, and pre-implemented linear
1025 algebra utilities [30].

1026 **SciPy:** The SciPy library is one of the core packages that make up the SciPy stack.
1027 It provides many user-friendly and efficient numerical routines, such as routines
1028 for numerical integration, interpolation, optimization, linear algebra, and statistics
1029 [45]. Two modules in particular form this libraries have covered an essential role
1030 in this project: the `SciPy.spatial.Voronoi` module for the computation of the 3D
1031 Voronoi decomposition, as mentioned in section 2.3, and the `SciPy.spatial.ConvexHull`
1032 module for the computation of 3D and 2D convex hulls (section 2.5).

1033 **PyTorch:** PyTorch is a rich ecosystem of tools and libraries geared toward Machine
1034 Learning and Deep Learning. The application of the style-transfer NN described
1035 in section 2.7 has required the use of this framework [31].

1036 **SALib:** The SALib is a library which collects many tools for the Sensitivity Analysis
1037 of parameters. In particular the `SALib.saltelli` submodel was used for the
1038 quasi-random numerical sampling in a three-dimensional box, and it has been
1039 described in section 2.4.

1040 **pnoise2:** pnoise2 contains many tools for the production of specific types of noise.
1041 The module `noise` was tweaked for the production of two-dimensional Perlin noise
1042 surfaces, and it has been introduced in section 2.6.

1043 **pyquaternion:** The pyquaternion library provides a framework for handling quaternions.
1044 It has been widely used in section 2.1 for the design of three-dimensional ramifications
1045 for handling multiple spatial rotations.

1046 Chapter 3

1047 ~~Tissues Model~~ Tissue Models 1048 Development

1049 The main goal of the present work, as stated before, is to recreate a three-dimensional
1050 virtual model of histological tissue as faithfully as possible and then, to perform planar
1051 sectioning on it to emulate virtually the traditional histological specimen preparation
1052 procedure. The creation of a model of such complex structures is definitely a high-
1053 level problem, and it has required a careful designing, made of subsequent stages of
1054 improvements. In section 3.1, I will describe all the necessary steps to create the model
1055 of a small region of pancreatic tissue, while in section 3.2 I will expose the steps I
1056 followed to build a model of dermal tissue. In section 3.3, instead, I will show the
1057 resulting synthetic images from the sectioning process performed on both the models
1058 and all the enrichments and processing necessary to give them the most realistic look I
1059 was able to recreate.

1060 3.1 Pancreatic Tissue Model

1061 The Pancreas is an internal organ of the human body, part of both the digestive system
1062 and the endocrine system. It acts as a gland with both endocrine and exocrine functions,
1063 and it is located in the abdomen behind the stomach. Its main endocrine duty is the
1064 secretion of hormones like insulin and glucagon which are responsible for the regulation of
1065 sugar levels in the bloodand the secretion of hormones, like insulin and glucagon. While,
1066 as. As a part of the digestive system instead it acts as an exocrine gland secreting
1067 pancreatic juice. The majority of pancreatic tissue has a digestive role, and the cells
1068 with this role form clusters (*acini*) around the small pancreatic ducts, and are arranged
1069 in lobes. The acinus secrete inactive digestive enzymes called zymogens into the small
1070 intercalated ducts which they surround, and then in the pancreatic blood vessels system
1071 [26]. In Figure 3.1 is shown a picture of the pancreas, with its structure and its placement

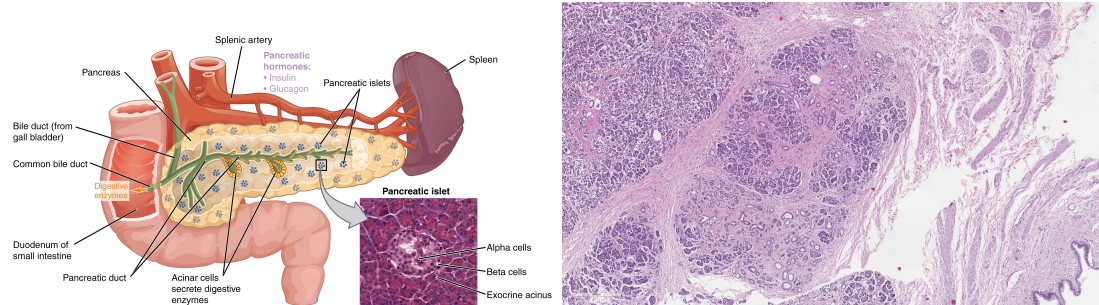


Figure 3.1: (left) A picture of pancreas' structure in its phisiologiacl context. In this picture is clearly visible the macroscopic structure and the glandular organization at microscopic level, and how it reflects in the histological sample. (right) A real pancreatic tissue sample with H&E staining.

1072 in the human body.

1073 All the tissue is actually rich in other important elements as the islets of Langerhans,
 1074 and sporadic connective tissue all over the structure, which are clearly visible in the
 1075 traditional histological specimens. In this first attempt of modelization from scratch
 1076 this second layer of complexity has not been already considered, and the main focus
 1077 has been to reflect only the main structural features on the virtual specimens. Given
 1078 pancreatic tissue's organization the first features I decided to put emphasis on were: 1)
 1079 The iterative (with a fractal-like behavior) ramification of blood vessels for the irrigation
 1080 of glandular acinus, 2) The space-filling distribution of acinus in the tissue, in fact, we
 1081 expect a homogeneous density in the organ and to not see *holes* at all inside it. In this
 1082 section I will describe step by step all the process I followed to create the model of a
 1083 portion of pancreatic tissue, and all the interesting pitfalls I overcame.

1084 3.1.1 2D Ramification

1085 The first step was took in two dimensions, and it was the choice of the right *structure*
 1086 to emulate the ramification of blood vessels in pancreatic tissue. The choice fell on a
 1087 particular parametric L-system, as the one shown in Figure 2.1, in section 2.2. This
 1088 structure is made of an iterative bifurcation of gradually shorter segments, with an angle
 1089 of $\pm 85^\circ$ respect the main direction. For a start I added some features to give a more
 1090 realistic look to the structure, which are all well represented in Figure 3.2:

- 1091 • A progressive thickness of the bifurcation's segments, starting from a thick main
 1092 branch that dwindle every junction. The idea is that the main blood vessel be-
 1093 comes gradually smaller becoming capillaries for single-cell irrigation.
- 1094 • A progressive randomness in the angular deflection at every fork. Perfectly repeated
 1095 angles are almost nonexistent in nature, so I decided to introduce an increasing

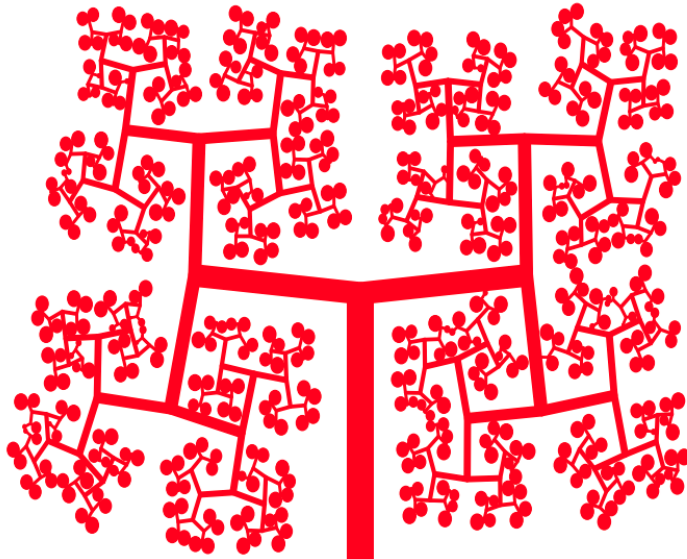


Figure 3.2: The development of the simple ramification in Figure 2.1, with some features to give it a more realistic look, like progressive thickness, angular noise in bifurcation and spheres at free ends of the ramification. The image is made using the tools exposed in section 2.2.

1096 indetermination in the angle of bifurcation from the main branch to the free ends
 1097 of the structures' branches.

- 1098 • Spheres at the ends of each branch, which acts as glandular acini. The maximum
 1099 radius is comparable to the length of the final segments.
- 1100 • A mechanism to avoid self-superimposition between branches and spheres. After
 1101 the insertion of noise, the cumulative effect on the final segments might lead different
 1102 branches to intersect. This is clearly a paradoxical situation, as real tissues
 1103 while growing naturally occupy the space in a gradual way.

1104 To produce the specific image in Figure 3.2 I used a particular setting of the tool
 1105 described in section 2.2, which have a greatly wider range of customization and could be
 1106 used to create many other different structures to the need.

1107 3.1.2 Expansion to 3D

1108 The successive step I followed was to expand this structure in three dimensions and fill
 1109 the space in each of the three directions. The idea to evolve the structure in Figure 3.2 is
 1110 simply to twist of 90° the ramification at every junction point, in such a way to exit the
 1111 previous belonging plane. However, putting into practice this development has not been

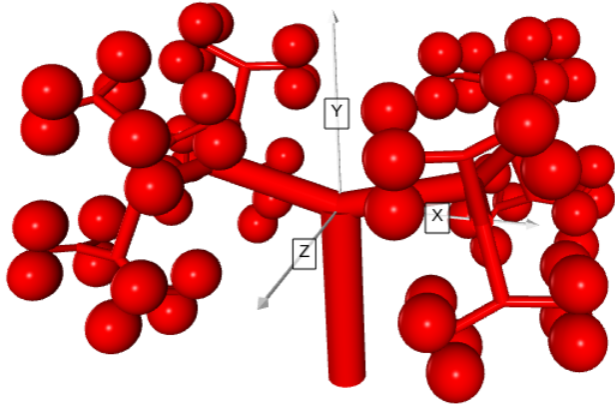


Figure 3.3: The three-dimensional expansion of the 2D ramification in Figure 3.2.

easy. The organization of the structure in a 3D space requires an appropriate system of reference for handling subsequent rotations in three dimensions. The best option for handling relative 3D rotations, often used in computer graphics and every kind of 3D modelization, are quaternions, as shown in section 2.1.

In this new structure, segments are replaced with cylinders, and circles are replaced with spheres. At every bifurcation to every cylinder are applied the following transformations:

- a contraction in its extensions, regulated by an adjustable parameter R .
- the usual deviation of $\pm 85^\circ$ respect to the direction of the parent branch.
- a 90° specific rotation along the axis of its parent branch.

The result of this procedure is a 3D ramification like the one in Figure 3.3, in which we can recognize a good coverage of the space defined by the structure's boundaries and immediate relation with the 2D structure in Figure 3.2. It should be noted that, in the further refinements of the model from now on, there won't be present the progressive angular indetermination on the direction of branches. Although it is a feature already implemented and working, it requires efficient control to avoid reciprocal overlapping between elements to produce a realistic structure. This second element has not been already developed and it would certainly enrich the representative power of the model.

As for the 2D ramification the production of this structure has required the implementation of a tool for the 3D generation with a greatly wider power, able to produce almost any type of three-dimensional iterative structure after the right adjustment, and with a high degree of customization. It is necessary to mention the fundamental tool

1134 which allowed me to accomplish this step of the development, which is the Python library
1135 VPython: a library for 3D graphics visualization. This library allows a convenient and
1136 powerful interface to draw many types of objects and to move them around in space,
1137 which has been priceless to orient my self in three dimensions while developing the model
1138 and to produce all the 3D images visible in this work.

1139 3.1.3 Subdivision in Cells

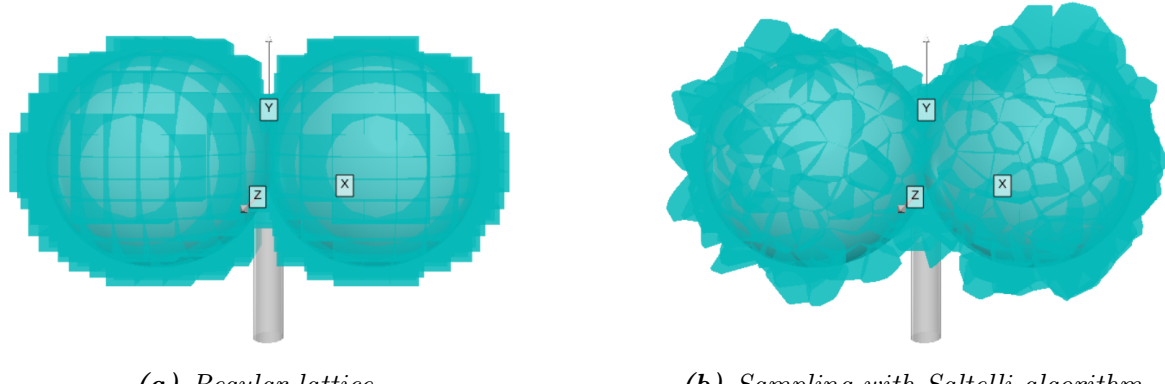
1140 Once the 3D backbone of the pancreatic tissue blood vessels ramification system has
1141 taken shape, the next step was to embed all this structure in a spatial partitioning
1142 process, to create the subdivision into single cells. To perform this important task I
1143 used a 3D Voronoi decomposition, as shown in section 2.3. Depending on the choice
1144 of the starting points, the Voronoi tessellation could be an excellent item to recreate
1145 individual cells because it could guarantee some important properties: all the regions
1146 are convex, adjacent, with similar size and volume, with different shapes, and without
1147 holes. These have been chosen as the most significant properties to be reflected in the
1148 first modelization of cells.

1149 As shown in section 2.3, the Voronoi decomposition strongly depends on the choice of
1150 the starting point. Points spread uniformly on a 3D regular lattice will produce a series
1151 of parallelepipeds repeated in the space. An example of uniform tessellation is shown in
1152 Figure 3.4a. On the other hand, a decomposition based on a quasi-random generated
1153 point can present all the good properties we mentioned before, including the diversity in
1154 shapes. In Figure 3.4b is shown an example of a Voronoi decomposition based on points
1155 sampled in a 3D with the Saltelli algorithm, in reference to section 2.4. Regardless of
1156 the points sampling technique, the boundaries of the sampling 3D box have been chosen
1157 to loosely contain the ramification.

1158 There are tough some delicate considerations to be highlighted about the decomposi-
1159 tion procedure. The first regards the most external pieces of the decomposition. Whilst
1160 the internal pieces are neatly bounded and defined, the most external layer instead is
1161 made on unbounded regions, which extend themselves to infinity. Those regions have
1162 clearly to be rejected, as it would be absurd for a cell to have an infinity volume. Typi-
1163 cally those unbounded regions are resized in order to adhere to some limiting boundaries,
1164 with an operation known as *cropping*. In Figure 3.5 is shown an example of circular crop-
1165 ping in a 2D Voronoi decomposition: all the regions which intersect the circumference
1166 have to be resized.

1167 The cropping operation in 3D is extremely complex, tough. Thus, a more simple and
1168 efficient, yet less elegant, technique has been used. Instead of resizing the regions which
1169 lie on the boundaries of the sampling region, those regions have directly been rejected.
1170 This process is really fast and it does not lead to any danger of representativity loss if
1171 the boundaries are loose enough and if the density of sampling is not too low.

1172 The other important consideration regards the density of sampling points. Increasing



(a) Regular lattice.

(b) Sampling with Saltelli algorithm.

Figure 3.4: Comparison between two Voronoi decompositions. The first (left) is created from a regular lattice of starting points, and every piece is exactly equal to all the others, creating a regular subdivision of the space. The second (right) is created instead from a sampling made following the Saltelli quasi-random algorithm. The pieces are all different in shape, but they all have similar sizes and volumes. In this pictures in particular have been shown only the pieces of the tessellation which lie in correspondence to the boundaries of the spheres underneath. While watching this picture one should immagine the decomposition extended similarly in all the space around the ramification, within certain boundaries, which loosely contains the structure. This limitation was necessary to enhance the interpretability of the image.

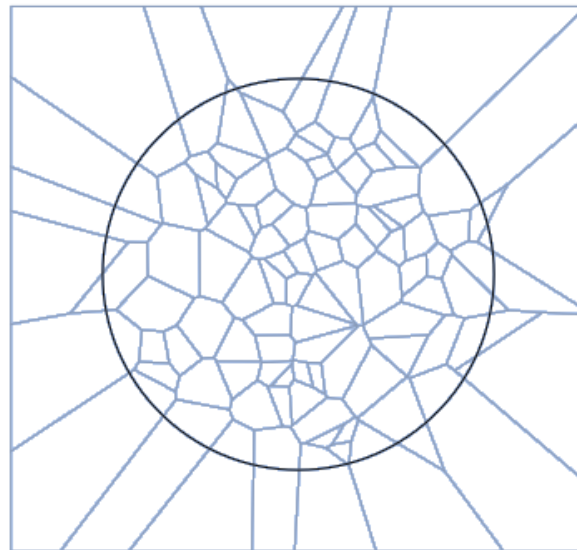


Figure 3.5: Example of circular cropping in a 2D Voronoi decomposition: all the regions which intersect the circumference have to be resized.

the number of points to be extracted from the same volume automatically the number of cells in the box will rise, and in contrast, their relative dimension will decrease. This is a key element of the model: a too rarified decomposition would not be able to reflect the complexity of the structure underneath, but a too crowded decomposition on the other side would lead to an unrealistic dimension of the cells in the tissue. Furthermore, this parameter has a huge influence on the computing time necessary to generate the model and to process it for the sectioning as will be shown in section 3.3. In almost all the applications so far, the density parameter has been tuned by eye, with a trial and error procedure. Although, a more rigorous way to adjust this parameter would be to consider the average dimension of the cells and make some microanatomical considerations to define the correct relative dimensions. The measure of the volume¹ of the decomposition's regions is an accessible parameter, thus an easy way to estimate the average linear dimension of the cells can be to approximate all the cells to cuboid seeing their volumes as $V \approx L^3$. Averaging all the L measures an estimate \hat{L} can be done. This average length may be compared to the length of the blood vessel ramification, allowing a good reference tool.

3.1.4 Cells Identity Assignment

The great power of creating all the models virtually is to know exactly the identity of every point in the structure. Although, this identity has to be reflected at the cellular level, assigning to every region a label. Imagining the Voronoi decomposition represented in Figure 3.4b extended to the entire box containing the ramification, good discrimination would distinguish three classes of cells: those which lie completely inside a sphere, those which lie completely outside a sphere, and those which lie on the boundaries of a sphere. In Figure 3.6 is shown a portion of the complete decomposition where the three classes of cells are reported with different colors: the internal cells in red, those on the boundaries in turquoise, and the external cells in gray.

In this particular case to find the relative position between every sphere in the structure and each cell it has been used a test on the proximity between the spheres' centers and the vertices of every polyhedral cell. If all the vertices of a region lie within a distance lower than the radius from the center of the same sphere then that region can be said to be an internal one. If none of the vertices lie within the radius distance from any center then that region is said to be external. In any other case, the region is said to be on the boundaries of some sphere, and this third label is assigned to it. As could be imagined the number of cells inside the volume can grow very quickly, and in the more rich ramifications also the number of spheres could be high. If we think that any polyhedron has a number of vertices of the order of 20/30 then it is clear that the number

¹The volume is expressed in the same arbitrary length unit of measures used during the ramification structure. This allows a coherent reference tool.

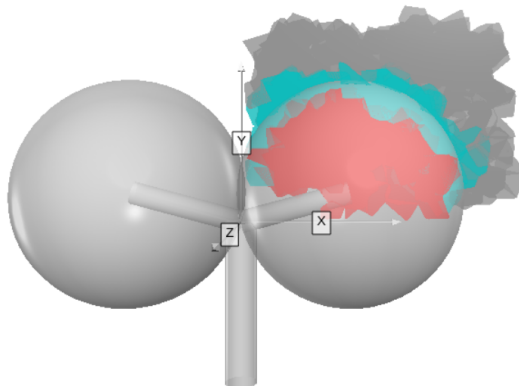


Figure 3.6: Portion of the complete Voronoi decomposition, showing the three different classes of cell in three different colors: the internal cells in red, those on the boundaries in turquoise and the external cells in gray.

of distance evaluations could grow very quickly, requiring some relevant computational power in the more extended simulations. In order to optimize this computation, I decided to use a python implementation of a K-dimensional Tree, which is a space-partitioning data structure especially suited for fast and optimized computation of distances [6]. A K-d Tree is an algorithm that iteratively binary splits the space: every node of the three could be thought as a splitting $(k - 1)$ -hyperplane dividing the space into two semi-hyperspace. The result is an optimized algorithm for repeated distance evaluations. As for many other tools, in my code I used a pre-implemented module `KDTree` from the `Scipy` library.

This procedure of labeling the regions is completely customizable, and it should be adapted to the specific application. By the way, the principle will always be to perform some sort of spatial consideration respect to the primary structure and assign all the interesting labels accordingly to the cells in the volume.

After labeling the cells in the decomposition the model is considered complete. Every enrichment to the structure should be reflected in some type of label for the cells, which are chosen as the fundamental unit in the model. As we will see in section 3.3 during the sectioning process in the produced image will be printed mainly the identity of the cells, hence any detail on a finer scale in the model would not be conveyed properly on the final image.

3.2 Dermal Tissue Model

Skin is the layer of soft, flexible outer tissue covering the body of a vertebrate animal, with the three main functions of protection, regulation, and sensation. Mammalian

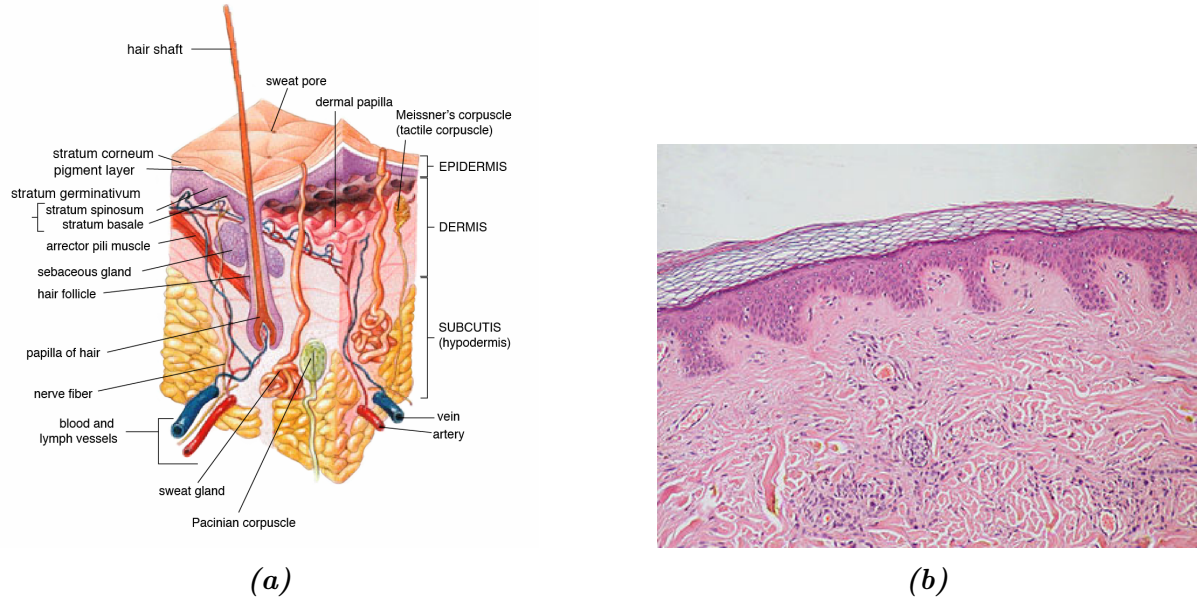


Figure 3.7: (left) Microanatomical description of a region of dermal tissue and all the interesting elements present in cutis, and subcutaneous layer. (right) An actual histological specimen from a sample of dermal tissue.

skin is composed of two primary layers: the epidermis, which provides waterproofing and serves as a barrier to infection, and the dermis, which serves as a location for the appendages of skin. The epidermis is composed of the outermost layers of the skin. It forms a protective barrier over the body's surface, responsible for keeping water in the body and preventing pathogens from entering, and is a stratified squamous epithelium, composed of proliferating basal and differentiated suprabasal keratinocytes. The dermis is the layer of skin beneath the epidermis that consists of connective tissue and cushions the body from stress and strain. The dermis provides tensile strength and elasticity to the skin through an extracellular matrix composed of collagen fibrils, microfibrils, and elastic fibers, embedded in hyaluronan and proteoglycans.

The modeling of the dermal tissue has followed analogous schedule respect to the previous model, hence many procedures and considerations have been repeated. The main target for this model was to recreate the stratification of different specific tissues in the section of a dermal sample. As clearly visible in Figure 3.7b in a dermal histological specimen one can distinguish the lighter and wider region of proper *dermal* tissue, underneath a more shallow and darker region of *epidermal* tissue. It is very interesting the boundary between those two regions, which can be seen as an irregular and smooth surface, populated of dermal lobes. On the other side of the epidermal layer lies a layer of *keratin*, with a smooth and regular boundary surface. Keratin is a family of fibrous structural proteins known as scleroproteins, a key structural material for hair, nails, and

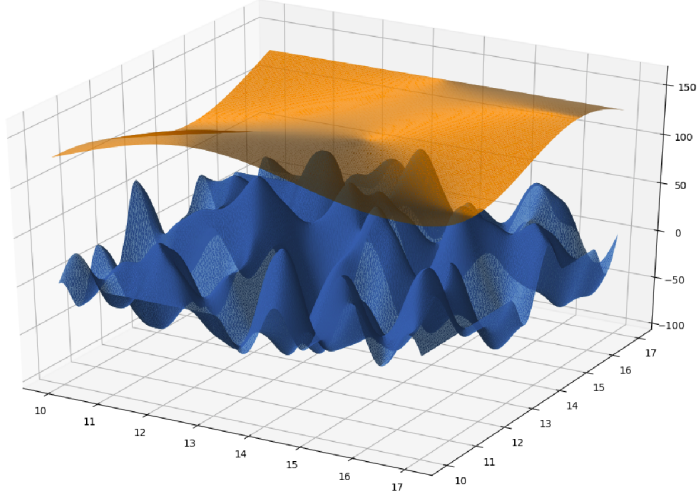


Figure 3.8: Pictures of two different Perlin noise surfaces used to separate dermal from epidermal tissue (blue) and epidermal from keratine layer (orange). The two surface are made by the same Perlin noise function, but the latter is stretched and compressed in order to have a more regular behavior.

1251 the outer layer of skin. The upper white region in Figure 3.7b instead is the support for
 1252 the samples to perform optical analysis, and has no histological meaning.

1253 1) Stratified Structure

1254 In order to represent faithfully the stratification of different tissue layers, I decided
 1255 to use one flat plane to separate epidermal tissue and the keratine layer and two
 1256 boundary surfaces modulated by a Perlin noise function on different scales for the
 1257 other two separations, as shown in Figure 3.8. As stated in section 2.6, after some
 1258 easy customization the generation of different Perlin noise surfaces is easy and
 1259 straightforward. By the way, to achieve the regularity and the smoothness of the
 1260 orange surface in Figure 3.8 it was needed a horizontal stretching.

1261 Following the scale of the image, the standard blue surface is created in a 7×7
 1262 square, while the orange surface has primarily been generated in a 1×1 square,
 1263 and then has been stretched to cover the same 7×7 square, multiplying the values
 1264 in its grid points respectively for the stretching factors $R_x = R_y = \frac{1}{7}$. In this
 1265 primary structure, there are many important parameters defining the surfaces, like
 1266 the distance between the two surfaes' average values and the amplitudes of the
 1267 peaks and the valleys of the surfaces. In its standard version the Perlin noise
 1268 covers the $[-1; 1]$ range, but with a simple multiplication for an amplitude factor
 1269 A_S the values can be adjusted. Those particular values have been adjusted after
 1270 some tries to recreate the proportions typical of a real specimen. To sum up, each
 1271 one of the two surfaces is stored as a discretized three-dimensional array, or better

1272 as an array of 3-tuples in the form $(x, y, f_{(x,y)})$, one tuple for every (x, y) node of
1273 the grid, while the discretization grid was the same for both the surfaces.

1274 2) Subdivision in Cells

1275 The subdivision in cells of the volume containing the structure has followed the
1276 exact same steps described in section 3.1, hence in this paragraph I will shortly
1277 resume the process. The first step is the definition of a suitable volume containing
1278 the structure. Then is the time for the generation of the decomposition's starting
1279 points according to a quasi-random number generation technique, as described in
1280 section 2.4. Afterward, the points are used as a base for the decomposition, and
1281 all the cells with undefined boundaries are rejected

1282 3) Cells Identity Assignment

1283 The identity assignment procedure instead has been customized for this particular
1284 application. In this model there are no *boundary* cells as the one lying on the
1285 spherical surfaces in the pancreatic model, thus there is no need for a test on the
1286 position of each vertex of every cell. In this model, the starting point for every
1287 Voronoi region has been used as a reference, and its relative position respect to the
1288 boundary surfaces was the discriminating factor for assessing the identity. In order
1289 to perform a coherent test on the relative position between the regions' center and
1290 the boundaries surfaces the positions of all the centers had to be discretized on
1291 the same grid onto which were defined the surfaces. The comparison with the flat
1292 horizontal plane defining the boundary between epidermal tissue and the keratine
1293 layer instead was simply a test on the z coordinate of the point: $z = f_{(x,y)} \leq \hat{z}_{plane}$.
1294 The result of this procedure is that every region is assigned a label corresponding
1295 to the belonging tissue layer: *D* for dermal, *E* for epidermal, *K* for keratine, and
1296 *V*, which stands for *void* for the white empty space above the sample.

1297 In this model, as in section 3.1, after the assignment of the identity to all the cells in
1298 the volume the modelization process is considered complete. Any sort of improvement
1299 and enrichment should be inserted during the structure designing phase and should be
1300 linked to an identity label.

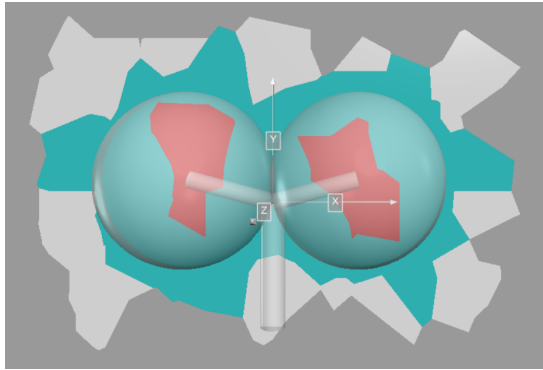
1301 3.3 Synthetic Images Production

1302 After the model is complete we have a three-dimensional representation of the tissue
1303 under study. The aim of the work is though to produce synthetic images from that
1304 structure, more precisely we want pairs of images composed of the synthetic-histological
1305 images and its related segmentation mask. The transition from 3D structure to a 2D
1306 image is the last step in the process, and it is inspired by the actual traditional technique
1307 for the preparation of the histological specimen, as described back in section 1.1.1. As
1308 the biopsy sample is treated and then sectioned with the microtome, the virtual model
1309 is sectioned in a random direction, producing an image representing the slice. This
1310 first image contains all the information of the section but its appearance is completely
1311 arbitrary and its look has nothing to share with a realistic sample. The original slice
1312 then acts perfectly as a segmentation mask, but some careful and dramatic makeover is
1313 needed to produce the final realistic looking image. In this section I will describe the
1314 general procedure to produce virtual slices from the two 3D virtual models described
1315 before in section 3 and the technique used to edit the images and give them the desired
1316 appearance.

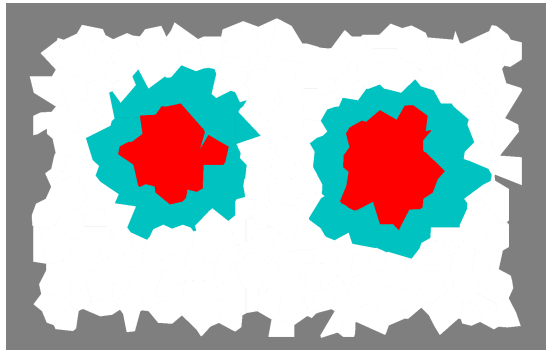
1317 3.3.1 Sectioning Process

1318 For any model created following the general procedure described in 3, even more so for
1319 the two particular models of pancreatic and dermal tissue, the sectioning process will
1320 be almost the same, and it will rely mainly on the algorithm for the general section of
1321 polyhedron described back in section 2.5. As stated before the models are essentially
1322 composed by labeled polyhedron spatially organized in a 3D volume. The ordered section
1323 of each polyhedron will yield all the polygons that shall be assembled in the final section.
1324 In Figure 3.9a is shown the three-dimensional representation of the section of a simple
1325 ramification, as the one in Figure 3.6. All the polygons that compose the section are
1326 drawn with the color correspondent to their label, following the same idea of Figure 3.6.
1327 In Figure 3.9b is printed the final result of the sectioning algorithm applied to the model,
1328 which will be the segmentation mask in the single pair of synthetic images. The colors
1329 in the produced slice match the colors used for the different identities in the 3D model.

1330 The simplest, yet over-abundant, way to proceed is to create the model in its entirety
1331 and subsequently choosing the sectioning plane. Afterward, it is necessary to select
1332 only the regions that intersect the plane and section them all. Actually, the test on the
1333 intersection passes through the check on the relative position of the polyhedron's vertices
1334 respect to the sectioning plane: if all the vertices lie on the same semi-space then the
1335 intersection would be null and the polyhedron is not of interest for that particular section.
1336 This procedure is exactly the first step of the algorithm in 2.5, thus the filtering on the
1337 regions is actually made during construction for optimization. The alternative method
1338 could be to choose in the first place the direction of the sectioning plane, and in second



(a) 2D polygonal sections represented in a 3D environment.



(b) The final section image, produced directly on a planar picture, skipping completely the 3D representation.

Figure 3.9: In this Figure is shown the idea of the correspondence between the section of a simple structure in the space and the correspondent section. The correspondence is not perfect for representation requirements, in fact the two images even if very similar are produced with two completely different methods. At the left an image of 2D polygonal section embeded in a 3D space, made using 3D visualization tools. At the right a simple image produced printing the polygons in a planar picture. Printing 2D polygons in a 3D space is much more complicated than one would think using the same tool used to produce the other images like Figure 3.6 and 3.4. This choice has been done for the sake of the overall homogeneity in pictures style.

1339 place to generate the model's decomposition only in the volume adjacent to that plane.
 1340 This method enables the sparing of a good amount of computation, without any negative
 1341 impact on the final result. The only delicate step is the choice of a wide enough region
 1342 of space around the plane, which doesn't compromise the representation.

1343 As a guarantee for richness and diversification among the images, there is the need
 1344 for some degree of controlled randomness in the sectioning process, for example in the
 1345 determination of the sectioning plane direction. All the sectioning process is then based
 1346 on a single starting *seed*, which determines the direction of the sectioning plane in a
 1347 deterministic way, and all the rest of the model is generated as a consequence. In this
 1348 way, all the possible angulations are equally probable and will be sampled in view of
 1349 multiple applications of this process. In Figure 3.10 are shown two different sections,
 1350 along two random planes on two simple ramified structures with four spheres.

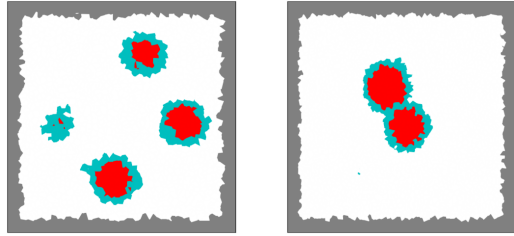


Figure 3.10: Two different section, along two random planes on two simple ramified structure with four spheres.

1351 3.3.2 Appearance Makeover

1352 After the application of the sectioning algorithm of the previous section, the image
 1353 which will act as a segmentation mask is ready. The last and most complex task that
 1354 remains is to transform the image and to give it a realistic look. I tried many different
 1355 transformations, more or less complicated, and there was not a final decision on which is
 1356 the best blend of them. In this section, I will describe them as an arsenal of possibilities
 1357 and show their impact on the images.

1358 Color Palette

1359 The first correction to do to the images will inevitably be a change in the colors
 1360 of the image. Gray, Turquoise, and Red are the perfect choice for label-colors but
 1361 act poorly as physiological colors. In Figure 3.11 is shown an example of an image
 1362 produced re-mapping the colors to a new palette, inspired to the coloring of the
 1363 real specimen in Figure 3.1 and 1.2, given by the traditional hematoxylin and eosin
 1364 staining process.

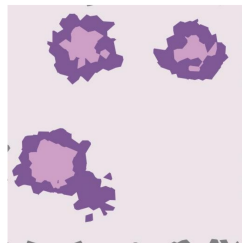


Figure 3.11: Example of images produced re-mapping the colors with a color palette inspired to a real H&E stained histological sample.

1365 Nuclei Projection

1366 Another fundamental processing needed was the projection of cells' nuclei on the
 1367 image. Usually, nuclei are clearly visible in histological samples and guide the

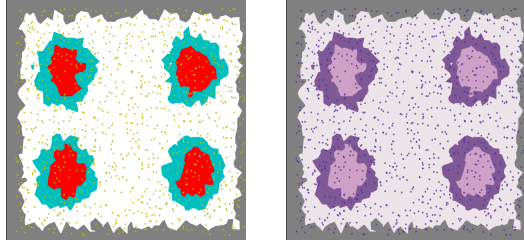


Figure 3.12: Nuclei projection on the image: (left) in yellow in the segmentation mask and (right) in purple in the image under makeover.

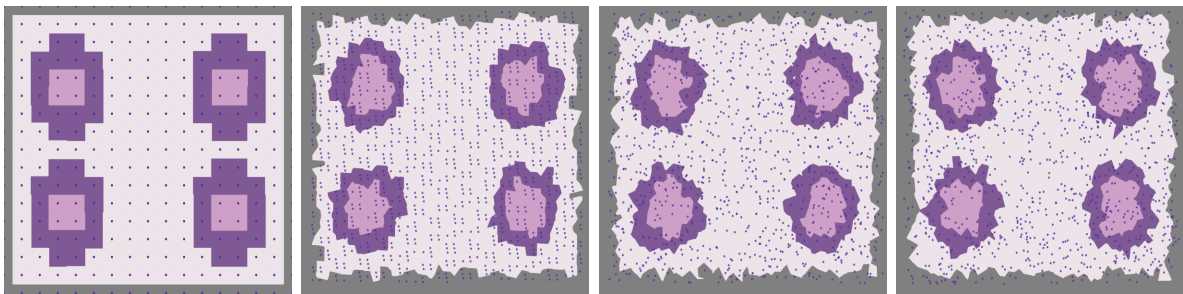


Figure 3.13: Four different sections produced with the same density on cells but with four different method for the sampling of starting decomposition's ponits (from left to right): • points sampled on a regular lattice, • sampling following a simple recursion sequence as the one in equation (2.12), • following the saltelli algorithm, • following a fully-random distribution.

analysis allowing to detect individual cells in the specimen. As a reference for the nucleus position the starting point of every polyhedral region has been used and projected on the sectioning plane as a little dark circle. The diameter of those circles as been chosen to be a submultiple (10%) of the linear estimated dimension \hat{L} of the cells in the decomposition².

Nuclei projection, among the other things, is an excellent tool to perceive the different effects obtained with different choices of quasi-random distributions or fully-random distributions (with reference to section 2.4). The different impact on the overall image is huge, and it really changes the overall sense of the image. In Figure 3.13 are reported four different sections, produced with the same density on cells but with four different methods for the sampling of starting decomposition's points.

Boundaries Projection

²Following the same logic of step 3 of section 3.1.

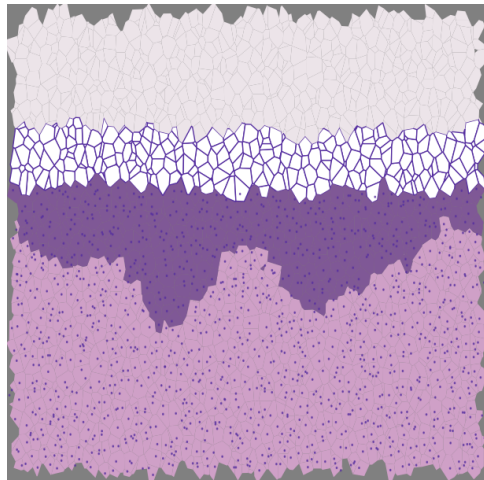


Figure 3.14: Example of images produced re-mapping the colors with a color palette inspired to a real H&E stained histological sample.

On the same wave of the previous tool, another operation that can help the appearance of an image is the projection of the boundaries of each (or just a part) of the polygonal sections. The drawing can be clearly tuned and customized depending on the specific necessities. In Figure 3.14 is shown an example of a section on the dermal tissue model in 3.2, in which the boundaries of all the cells have been lightly marked, and the boundaries of the cells in the keratine layer have been heavily marked instead.

Blurring Effects

In all the images produced so far the boundaries between polygonal sections are perfectly sharp and without any smudge. To give a more realistic feeling to those pictures I tried different forms of blurring. As a first try, I applied a Gaussian blurring filter, which is an extremely common blurring operation in computer vision, which consists of a simple discrete convolution with a 2D Gaussian kernel. The effect is a regular and diffuse blur all over the image, as in Figure 3.15a. The second blurring effect I implemented was based instead on the averaging of parallel and adjacent slices on the same model. This method is inspired by the real sectioning technique (section 1.1.1), in which every slice is not an infinitesimal layer of matter, but a finite sample, which suffers from mechanical dragging during the process. The idea is that the average between three or more slices equally spaced above and below the *main* slice should recreate a realistic blurring effect. An example of an image produced with this process is shown in Figure 3.15b.

Perlin RGB Noise

A further attempt to give visual texture to the image was done using again the

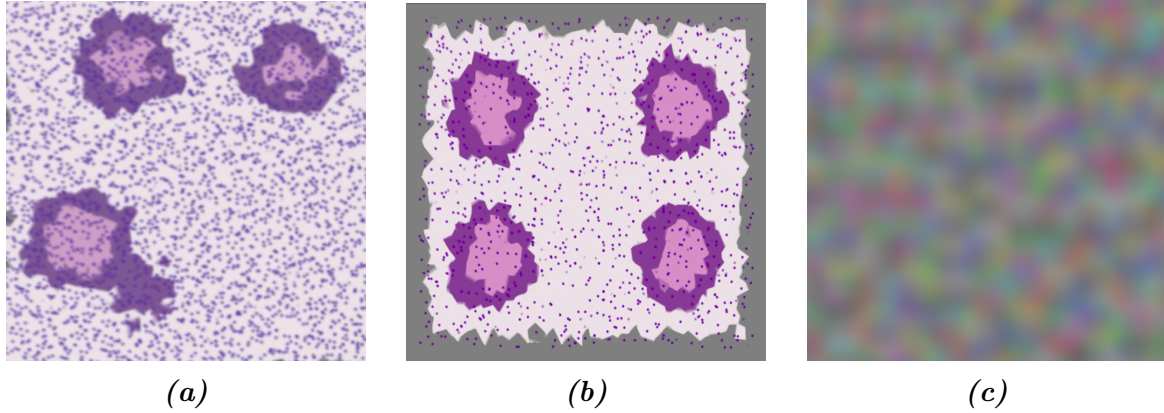


Figure 3.15: The two blurring effects used in this work: (left) A standard Gaussian-filter blur and (center) a specific blur introduced averaging adjacent parallel slices on the same image, (right) an example of RGB color noise built joining three different Perlin noise surfaces, one for each color channel.

Perlin noise, described in section 2.6. The idea is to create some fluctuation among the color channels of the image around the sharp values of the image produced by the sectioning algorithm. From a practical point of view, I created three different and independent Perlin noise surfaces, one for every color channel (Red, Green, and Blue), and added them to create an RGB noise on the image. An example of the resulting image is shown in Figure 3.15c.

Style Transfer

This last tool I will describe is the most sophisticated so far. It consists of the application of a style-transfer neural network (STNN) on the image obtained through the sectioning process, for the implantation of the visual texture from a real sample of the corresponding tissue. Style-transfer NNs, and their functioning, have been described in detail in section 2.7, and here I will cover just the particular applications on the two type of section produced.

The first manipulation I report is the one on a section from the pancreatic tissue model. The image of which to conserve the visual content is a section with some simple pre-processing picked from the ones described before (Figure 3.16a): a more accurate color palette, the projection of nuclei, and the average on five adjacent slices. The image from which to pick the style, thus the visual texture, is a portion of an actual histological sample of the pancreas, and it is shown in Figure 3.16b. The application of the STNN yields a hybrid image, shown in Figure 3.16c. The second application was made on a section on dermal tissue. The three content, style and styled images are shown respectively in Figure 3.17a, 3.17b, and 3.17c.

In Figures 3.16, and 3.17 are reported the best results among all the different tests

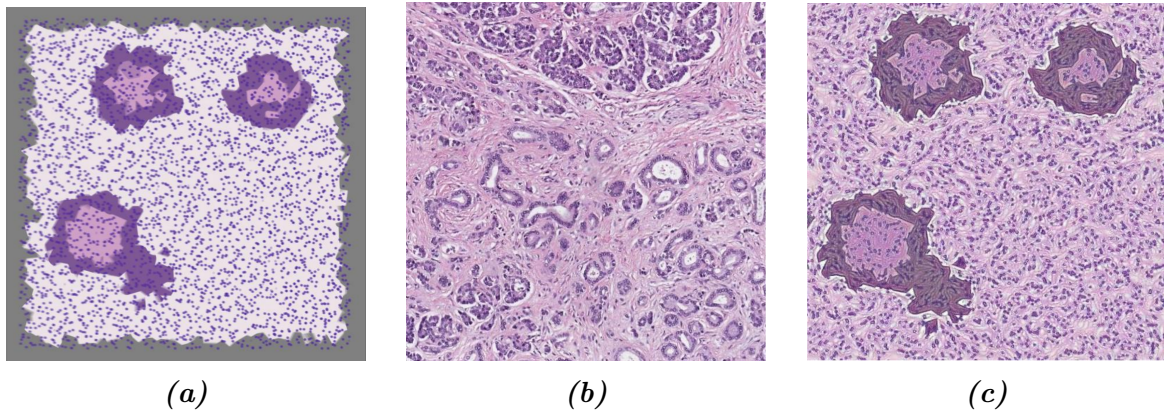


Figure 3.16: Application of the style-transfer NN on a section of the pancreatic tissue model: 3.16a the content image, 3.16b the style image, 3.16c the hybrid resulting image.

made on the sections. I made different tries on the same image with different processing before the manipulation with the STNN, to see the impact of the different adjustment on the resulting styled image. It turned out that the presence of nuclei is essential to give a homogeneous texture to the image and avoid unrealistic artifacts. On the other hand, the choice of the color palette has a way lighter effect than what one would think: the model yields almost the same result with a grey-levels image or with any other palette.

It is interesting to notice the timing cost of this style transfer operation. While all the other manipulation described in this chapter requires a very short time (seconds) to be applied, and are in practice *instantaneous*, the transfer of style is a way more robust operation, which implies the finalization of the training of a pre-trained neural network. On a computer with the technical specification described in section 2.8 this operation instead took minutes, which is a time two full orders of magnitude greater.

It should be noted that the presented results are obtained from the application of a pre-trained STNN model. The development of a specialized model for histological texture transfer could improve extremely the ability to produce realistic images, way further the present results.

One single complete application of the process consists then in the generation of a tissue model, in the sectioning along a random section plane, and in the processing of the image, in order to produce the pair of ground-truth image and the synthetic histological image. The target is to apply over and over this process to collect the necessary amount of images and constitute an entire dataset. An important feature to have for the process is thus a complete automatization, in order to scale up the

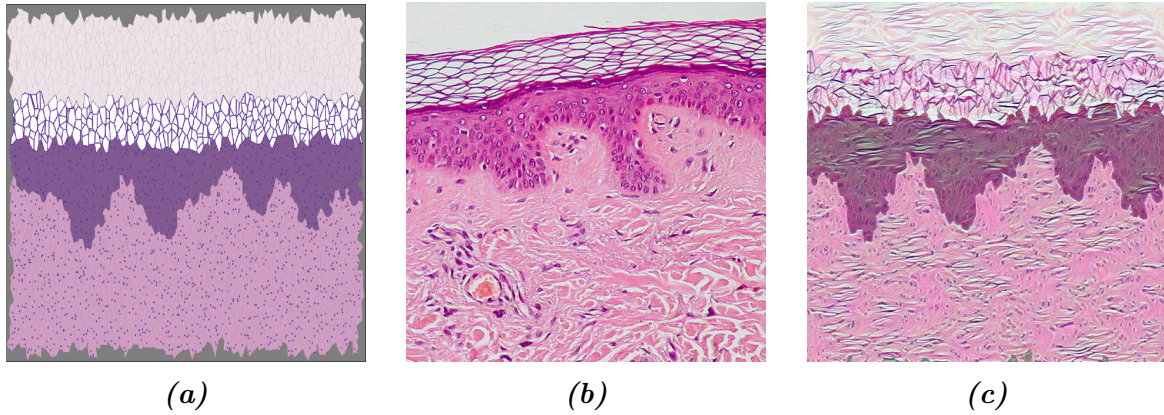


Figure 3.17: Application of the style-transfer NN on a section of the dermal tissue model: 3.17a the content image, 3.17b the style image, 3.17c the hybrid resulting image.

generation of images, possibly even in parallel computation. For this purpose, I created a pipeline workflow interface for the image generation, with an automatized harmonization of every piece of the process. The generation now requires just to fill a configuration file in which writes all the specific characteristics of the images: the type of structure, its features, the desired processing on the images, and eventually the random seeds for a supervised generation. In Figure 3.18 is reported a small scale example of a dataset produced with multiple automatized applications of the generation tool on a ramified structure inspired to a pancreatic tissue model. It is clear the correspondence between segmentation mask and synthetic histological images, and the diversification given by the supervised randomness on the generation.

The actual tool used for the set up of a working pipeline was the `Snakemake` [24] workflow management system, which is a python-based tool to create reproducible and scalable data analyses.

3.3.3 Alternative Works on Synthetic Histological Images Generation

As a conclusion to this chapter, I want to make an overview of some other interesting works on the generation

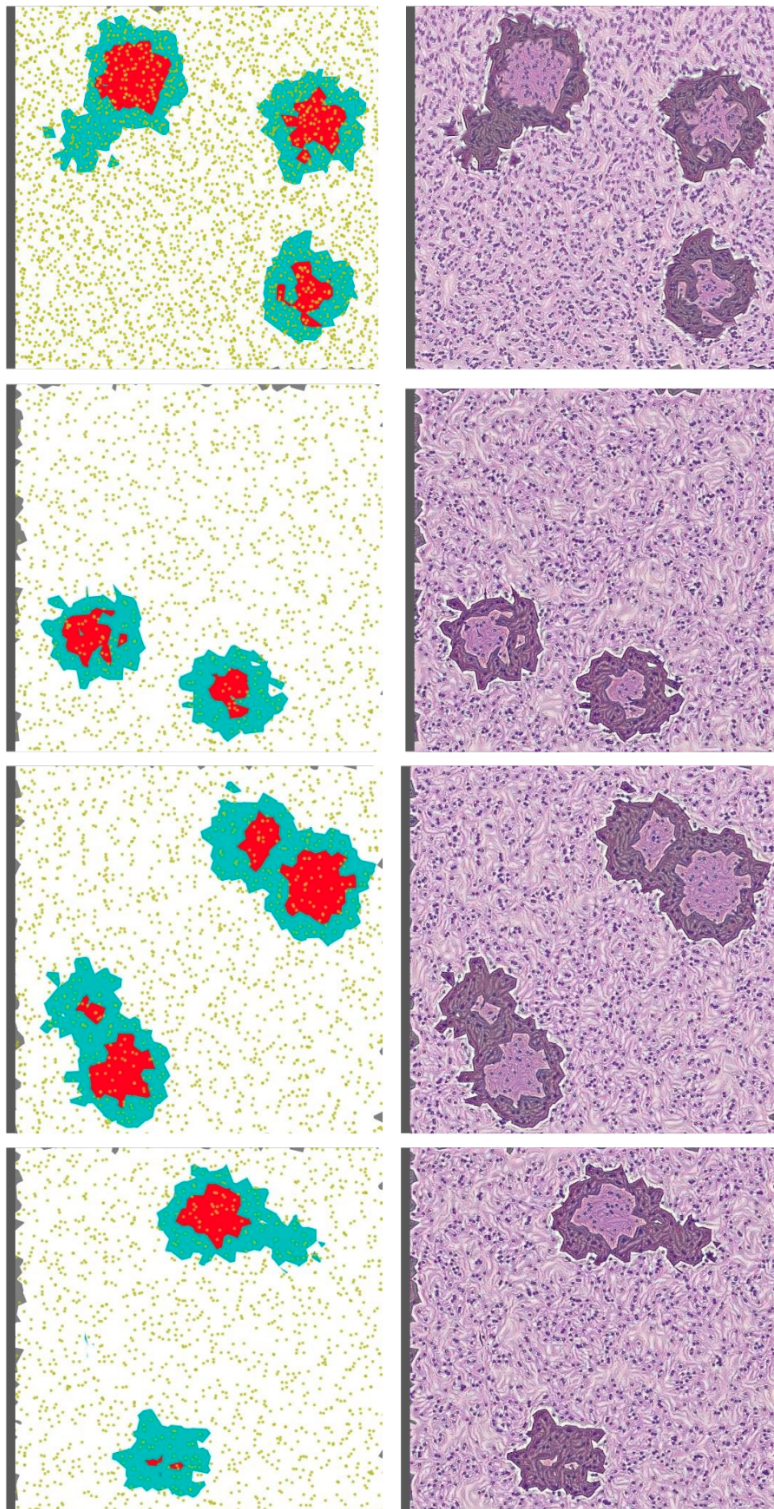


Figure 3.18: Small scale example of dataset produced with multiple automated applications of the generation tool on a ramified structure inspired to a pancreatic tissue model.

1467 Conclusions

1468 In this project, I face the problem of synthetic histological images, which have followed
1469 completely different paths and strategies.

1470 The first work I want to cite is a work from Ben Cheikh *et al.* from 2017 [9]. In
1471 image generation for the purpose of training Neural Networks for the segmentation of
1472 real histological images. The manual analysis of histological specimen is a complex,
1473 time consuming, and expensive task and nevertheless it is a pillar of countless diagnostic
1474 techniques. Any form of support for this procedure hence is welcome and endorsed by
1475 the health-care system. In particular, in this work, they present a methodology for the
1476 generation of synthetic images of different types of breast carcinomas. They propose a
1477 method completely based on two-dimensional morphology operation, as successive image
1478 dilations and erosions. With the modulation of a very restricted number of parameters,
1479 regulating the abundance of the objects, their distribution in the image, and their shapes
1480 they are able to reconstruct realistic images reflecting different histological situations.
1481 In Figure 2 is shown an example of generated material besides a real histological H&E
1482 stained sample. Starting from a generated segmentation mask which defines the *tumoral*
1483 *pattern* the production of the synthetic image passes through successive steps, as the
1484 generation of characteristic collagen fibers around the structure, the injection of all the
1485 immune system cells, and some general final refinements. I focus on the problem of
1486 histological specimens segmentation. The most advanced algorithms for image segmentation
1487 are based on Deep Learning and requires the training of extensive and complex neural
1488 networks. One of the toughest hurdles to overcome for the training of those NN is the
1489 abundance and the quantity of pre-labeled examples of segmentation on real histological
1490 samples. The collection of hundreds of hand-labeled histological samples, with pixel-level
1491 precision, is virtually impossible. This work thus proposes a methodology to generate,
1492 in a completely automatic way, synthetic pre-labeled histological-like images, that can
1493 be used as training material for a NN.

1494 Example of generated tumoral pattern (left), which acts as segmentation mask, of
1495 generated image (center) and a real example of the tissue to recreate. From [9]. The
1496 method I propose consists of the recreation of the traditional histological specimens'
1497 preparation, and it is based on the sectioning of a 3D virtual model of a region of
histological tissue. The virtual 3D model of a region of a particular type of human tissue

1499 is built after physical and physiological considerations. The model is then subject to a
1500 virtual sectioning operation, which yields the synthetic sampling of the virtual tissue in
1501 which the histological identity of every pixel is perfectly known. This first image will act
1502 as a segmentation mask for a second, realistic image. In fact, on top of this first image
1503 are applied several aesthetical processing and refinements and the final product is the
1504 synthetic histological-like image. The pair made of the two images is then perfect for
1505 the supervised learning of a NN oriented toward the segmentation of histological images.
1506 The production of each pair of images is completely automatic and it does not require the
1507 intervention of any human operator, it is thus a scalable process that can produce a great
1508 abundance of images. The quality of the images is directly connected to the richness and
1509 the quality of the model. The perfect modelization of a region of tissue, let's say human
1510 pancreatic tissue, is by far out of reach for this, hence the richness and the fidelity of the
1511 produced images are inevitably lower than the real sample. Nevertheless, the quality of
1512 the produced images is sufficient to perform the preliminary phase of the training of a
1513 NN following a training strategy known as curriculum learning. This learning process
1514 consists of giving the NN a copious quantity of lower complexity level example in the
1515 first instance, reserving the few and sophisticated real hand-labeled histological samples
1516 for the finalization of the training.

1517 The first chapter of this thesis is devoted to the contextualization of the present
1518 work. It is offered a description of how the histological samples are obtained after
1519 a tissue biopsy and how the digitalization process of the images works. The reader
1520 is then introduced to the framework of Deep Learning, its fundamental aspect, and
1521 components. The concept of neural network is exposed and it is given the general idea
1522 underneath the training of a DL-based model. The chapter comes to an end with a
1523 general introduction to the segmentation task in computer vision, and how it is currently
1524 tackled with state-of-the-art algorithms.

1525 The second ~~work I want to mention is base on a DL base technique, which approaches~~
1526 ~~synthetic image generation using a specific eGAN architecture inspired to the “U-net”~~
1527 ~~[38] model described back in Figure 1.13 in section 1.3.1. This model works with Ki67~~
1528 ~~stained samples of breast cancer tissue~~ chapter collects all the details of every less common
1529 technical tool I used during the design of this project. A brief theoretical introduction is
1530 proposed for every item besides the thorough description of its practical use. Some of the
1531 arguments touched by this chapter are quaternions, quasi-random number generation,
1532 Voronoi decomposition, style transfer neural networks. In this chapter, a section is
1533 devoted to the description of a general methodology for computing the 2D section of an
1534 arbitrary three-dimensional polyhedron. The algorithm here described has been devised
1535 and implemented all by my self, and then inserted in the workflow of the project. As
1536 a conclusion for this chapter, I describe the working environment I built for developing
1537 this project and I mention all the code libraries I employed in my work.

1538 The third chapter is the center of this work, and it ~~is able to generate high-fidelity~~
1539 ~~images starting from a given segmentation mask. Those starting segmentation masks~~

1540 tough are obtained through the processing of other real histological samples, via a
1541 nuclei-detection algorithm. The differences between real and synthetic samples are
1542 imperceptible, and the material generated in this work has effectively fooled experts,
1543 who qualified it has indistinguishable from the real one. In Figure 3 an example of a real
1544 image, a generated one, and their corresponding segmentation mask.

1545 Example of generated tumoral pattern (left), which acts as segmentation mask, of
1546 generated image (center) and a real example of the tissue to recreate. From [38].

1547 contains the description of all the design choices, and the steps I followed for the
1548 development of the two human tissue models I propose: the first of pancreatic tissue and
1549 the second of dermal tissue. The development has required the harmonization of many
1550 different technical aspects and mathematical tools. The first section is then dedicated
1551 to the description of the pancreatic tissue model, which passes through different steps:
1552 from a two-dimensional ramification taken as inspiration for the behavior of blood vessels
1553 to the complete three-dimensional model, with its subdivision in labeled cells. The
1554 second section is occupied by the description of the dermal tissue model, following the
1555 same spirit. The third section instead contains a thorough description of the method to
1556 perform the sectioning onto a virtual model and how to process the resulting images.
1557 It is necessary to perform several alternative processing and adjustment to achieve the
1558 desired aspect both for the segmentation mask image and for the histological-like image
1559 after the sectioning process.

1560 The method for the generation of datasets of synthetic images I propose in my thesis
1561 work is a self-supporting project and it is formally consistent. By the way, there are
1562 many possibilities for improvement and enrichment for the project. One first aspect to
1563 strengthen could be the richness of the models: adding more elements in the structure,
1564 and refining their representation of the tissue at the cellular level. This would lead
1565 to a better quality of the synthetic images, that would assist the training of NN in
1566 more and different applications. Another aspect that lends itself to improvements in the
1567 development of a dedicated style transfer NN targeting the histological texture transfer,
1568 which could lead to interesting signs of progress in the quality of image generation. There
1569 is also the intention to perform an actual attempt of NN training on the images produced
1570 with this process. This would complete conceptually the idea underneath the project
1571 and would be an excellent opportunity to detect weaknesses and to draw up possible
1572 lines of development. The repeated application of the generation method would allow
1573 the building of entire datasets suitable for the training of DL-based models.

₁₅₇₄

Bibliography

- ₁₅₇₅ [1] Abien Fred Agarap. Deep learning using rectified linear units (relu), 2018.
- ₁₅₇₆ [2] Salah Alheejawi, Mrinal Mandal, Hongming Xu, Cheng Lu, Richard Berendt, and
₁₅₇₇ Naresh Jha. Deep learning-based histopathological image analysis for automated
₁₅₇₈ detection and staging of melanoma. In *Deep Learning Techniques for Biomedical*
₁₅₇₉ and *Health Informatics*, pages 237–265. Elsevier, 2020.
- ₁₅₈₀ [3] J. Alsayednoor and P. Harrison. Evaluating the performance of microstructure
₁₅₈₁ generation algorithms for 2-d foam-like representative volume elements. *Mechanics*
₁₅₈₂ of *Materials*, 98:44 – 58, 2016.
- ₁₅₈₃ [4] Hani A Alturkistani, Faris M Tashkandi, and Zuhair M Mohammedsaleh. Histolog-
₁₅₈₄ ical stains: A literature review and case study. *Global Journal of Health Science*,
₁₅₈₅ 8(3):72, June 2015.
- ₁₅₈₆ [5] Yoshua Bengio, Jérôme Louradour, Ronan Collobert, and Jason Weston. Curricu-
₁₅₈₇ lum learning. In *Proceedings of the 26th Annual International Conference on Ma-*
₁₅₈₈ *chine Learning*, ICML '09, page 4148, New York, NY, USA, 2009. Association for
₁₅₈₉ Computing Machinery.
- ₁₅₉₀ [6] Jon Louis Bentley. Multidimensional binary search trees used for associative search-
₁₅₉₁ ing. *Commun. ACM*, 18(9):509517, September 1975.
- ₁₅₉₂ [7] R. W. Brockett. Robotic manipulators and the product of exponentials formula.
₁₅₉₃ In P. A. Fuhrmann, editor, *Mathematical Theory of Networks and Systems*, pages
₁₅₉₄ 120–129, Berlin, Heidelberg, 1984. Springer Berlin Heidelberg.
- ₁₅₉₅ [8] C. G. BROYDEN. The Convergence of a Class of Double-rank Minimization Algo-
₁₅₉₆ rithms 1. General Considerations. *IMA Journal of Applied Mathematics*, 6(1):76–90,
₁₅₉₇ 03 1970.
- ₁₅₉₈ [9] Bassem Ben Cheikh, Catherine Bor-Angelier, and Daniel Racoceanu. A model of
₁₅₉₉ tumor architecture and spatial interactions with tumor microenvironment in breast
₁₆₀₀ carcinoma. In Metin N. Gurcan and John E. Tomaszewski, editors, *Medical Imaging*

- 1601 2017: *Digital Pathology*, volume 10140, pages 73 – 80. International Society for
 1602 Optics and Photonics, SPIE, 2017.
- 1603 [10] Anna Choromanska, Benjamin Cowen, Sadhana Kumaravel, Ronny Luss, Mattia
 1604 Rigotti, Irina Rish, Brian Kingsbury, Paolo DiAchille, Viatcheslav Gurev, Ravi
 1605 Tejwani, and Djallel Bouneffouf. Beyond backprop: Online alternating minimization
 1606 with auxiliary variables, 2018.
- 1607 [11] Siddharth Singh Chouhan, Ajay Kaul, and Uday Pratap Singh. Image segmentation
 1608 using computational intelligence techniques: Review. *Archives of Computational
 1609 Methods in Engineering*, 26(3):533–596, February 2018.
- 1610 [12] Marius Cordts, Mohamed Omran, Sebastian Ramos, Timo Rehfeld, Markus En-
 1611 zweiler, Rodrigo Benenson, Uwe Franke, Stefan Roth, and Bernt Schiele. The
 1612 cityscapes dataset for semantic urban scene understanding. *CoRR*, abs/1604.01685,
 1613 2016.
- 1614 [13] Angel Cruz-Roa, Ajay Basavanhally, Fabio Gonzlez, Hannah Gilmore, Michael Feld-
 1615 man, Shridar Ganesan, Natalie Shih, John Tomaszewski, and Anant Madabhushi.
 1616 Automatic detection of invasive ductal carcinoma in whole slide images with convo-
 1617 lutional neural networks. *Progress in Biomedical Optics and Imaging - Proceedings
 1618 of SPIE*, 9041, 02 2014.
- 1619 [14] Alessandro d’Agostino. Dataset generation for the training of neural networks ori-
 1620 ented toward histological image segmentation, april 2020.
- 1621 [15] J. Deng, W. Dong, R. Socher, L. Li, Kai Li, and Li Fei-Fei. Imagenet: A large-scale
 1622 hierarchical image database. In *2009 IEEE Conference on Computer Vision and
 1623 Pattern Recognition*, pages 248–255, 2009.
- 1624 [16] J. Deng, W. Dong, R. Socher, L.-J. Li, K. Li, and L. Fei-Fei. ImageNet: A Large-
 1625 Scale Hierarchical Image Database. In *CVPR09*, 2009.
- 1626 [17] Mark Everingham, Luc Van Gool, Christopher KI Williams, John Winn, and An-
 1627 drew Zisserman. The pascal visual object classes (voc) challenge. *International
 1628 journal of computer vision*, 88(2):303–338, 2010.
- 1629 [18] Leon A. Gatys, Alexander S. Ecker, and Matthias Bethge. A neural algorithm of
 1630 artistic style, 2015.
- 1631 [19] Sepp Hochreiter and Jürgen Schmidhuber. Long short-term memory. *Neural com-
 1632 putation*, 9(8):1735–1780, 1997.
- 1633 [20] Phillip Isola, Jun-Yan Zhu, Tinghui Zhou, and Alexei A. Efros. Image-to-image
 1634 translation with conditional adversarial networks, 2016.

- 1635 [21] Diederik P. Kingma and Jimmy Ba. Adam: A method for stochastic optimization,
1636 2014.
- 1637 [22] Alex Krizhevsky. Learning multiple layers of features from tiny images. Technical
1638 report, 2009.
- 1639 [23] Alex Krizhevsky, Ilya Sutskever, and Geoffrey E Hinton. Imagenet classification with
1640 deep convolutional neural networks. In *Advances in neural information processing*
1641 *systems*, pages 1097–1105, 2012.
- 1642 [24] Johannes Kster and Sven Rahmann. Snakemakea scalable bioinformatics workflow
1643 engine. *Bioinformatics*, 28(19):2520–2522, 08 2012.
- 1644 [25] Aristid Lindenmayer. Mathematical models for cellular interactions in development
1645 ii. simple and branching filaments with two-sided inputs. *Journal of theoretical*
1646 *biology*, 18(3):300–315, 1968.
- 1647 [26] Daniel. Longnecker. Anatomy and histology of the pancreas, 2014.
- 1648 [27] Shervin Minaee, Yuri Boykov, Fatih Porikli, Antonio Plaza, Nasser Kehtarnavaz,
1649 and Demetri Terzopoulos. Image segmentation using deep learning: A survey, 2020.
- 1650 [28] Muhammad Niazi, Thomas Tavolara, Vidya Arole, Douglas Hartman, Liron Pan-
1651 tanowitz, and Metin Gurcan. Identifying tumor in pancreatic neuroendocrine neo-
1652 plasms from ki67 images using transfer learning. *PLOS ONE*, 13:e0195621, 04 2018.
- 1653 [29] Arild Nkland and Lars Hiller Eidnes. Training neural networks with local error
1654 signals, 2019.
- 1655 [30] Travis E Oliphant. *A guide to NumPy*, volume 1. Trelgol Publishing USA, 2006.
- 1656 [31] Adam Paszke, Sam Gross, Francisco Massa, Adam Lerer, James Bradbury, Gre-
1657 gory Chanan, Trevor Killeen, Zeming Lin, Natalia Gimelshein, Luca Antiga, Alban
1658 Desmaison, Andreas Kopf, Edward Yang, Zachary DeVito, Martin Raison, Alykhan
1659 Tejani, Sasank Chilamkurthy, Benoit Steiner, Lu Fang, Junjie Bai, and Soumith
1660 Chintala. Pytorch: An imperative style, high-performance deep learning library,
1661 2019.
- 1662 [32] Allan Pinkus. Approximation theory of the mlp model in neural networks. *Acta*
1663 *Numerica*, 8:143195, 1999.
- 1664 [33] Prabu Ravindran, Adriana Costa, Richard Soares, and Alex C Wiedenhoeft. Clas-
1665 sification of cites-listed and other neotropical meliaceae wood images using convo-
1666 lutional neural networks. *Plant methods*, 14(1):1–10, 2018.

- 1667 [34] Olaf Ronneberger, Philipp Fischer, and Thomas Brox. U-net: Convolutional net-
1668 works for biomedical image segmentation. *CoRR*, abs/1505.04597, 2015.
- 1669 [35] Juan Rosai. Why microscopy will remain a cornerstone of surgical pathology. *Lab-*
1670 *oratory Investigation*, 87(5):403–408, April 2007.
- 1671 [36] Andrea Saltelli. Making best use of model evaluations to compute sensitivity indices.
1672 *Computer Physics Communications*, 145(2):280 – 297, 2002.
- 1673 [37] Andrea Saltelli, Paola Annoni, Ivano Azzini, Francesca Campolongo, Marco Ratto,
1674 and Stefano Tarantola. Variance based sensitivity analysis of model output. design
1675 and estimator for the total sensitivity index. *Computer Physics Communications*,
1676 181(2):259 – 270, 2010.
- 1677 [38] Caglar Senaras, Muhammad Khalid Khan Niazi, Berkman Sahiner, Michael P. Pen-
1678 nell, Gary Tozbikian, Gerard Lozanski, and Metin N. Gurcan. Optimized generation
1679 of high-resolution phantom images using cGAN: Application to quantification of ki67
1680 breast cancer images. *PLOS ONE*, 13(5):e0196846, May 2018.
- 1681 [39] David F Shanno. Conditioning of quasi-newton methods for function minimization.
1682 *Mathematics of computation*, 24(111):647–656, 1970.
- 1683 [40] Karen Simonyan and Andrew Zisserman. Very deep convolutional networks for
1684 large-scale image recognition, 2014.
- 1685 [41] Sandro Skansi. *Introduction to Deep Learning: From Logical Calculus to Artificial*
1686 *Intelligence*. Springer Publishing Company, Incorporated, 1st edition, 2018.
- 1687 [42] I.M. Sobol. Uniformly distributed sequences with an additional uniform prop-
1688 erty. *USSR Computational Mathematics and Mathematical Physics*, 16(5):236 –
1689 242, 1976.
- 1690 [43] I.M Sobol. Global sensitivity indices for nonlinear mathematical models and their
1691 monte carlo estimates. *Mathematics and Computers in Simulation*, 55(1):271 – 280,
1692 2001. The Second IMACS Seminar on Monte Carlo Methods.
- 1693 [44] M Titford. The long history of hematoxylin. *Biotechnic & Histochemistry*, 80(2):73–
1694 78, 2005.
- 1695 [45] Pauli Virtanen, Ralf Gommers, Travis E. Oliphant, Matt Haberland, Tyler Reddy,
1696 David Cournapeau, Evgeni Burovski, Pearu Peterson, Warren Weckesser, Jonathan
1697 Bright, Stéfan J. van der Walt, Matthew Brett, Joshua Wilson, K. Jarrod Millman,
1698 Nikolay Mayorov, Andrew R. J. Nelson, Eric Jones, Robert Kern, Eric Larson,
1699 CJ Carey, İlhan Polat, Yu Feng, Eric W. Moore, Jake VanderPlas, Denis Laxalde,

1700 Josef Perktold, Robert Cimrman, Ian Henriksen, E. A. Quintero, Charles R Harris,
1701 Anne M. Archibald, Antônio H. Ribeiro, Fabian Pedregosa, Paul van Mulbregt,
1702 and SciPy 1. 0 Contributors. SciPy 1.0: Fundamental Algorithms for Scientific
1703 Computing in Python. *Nature Methods*, 17:261–272, 2020.

1704 [46] Georges Voronoi. Nouvelles applications des paramètres continus à la théorie des
1705 formes quadratiques. premier mémoire. sur quelques propriétés des formes quadra-
1706 tiques positives parfaites. *Journal für die reine und angewandte Mathematik (Crelles
1707 Journal)*, 1908:102 – 97.